48

Quantum-Dot Nanolasers

Christopher Gies
Michael Lorke
Frank Jahnke and
Weng W. Chow

48.1 Going Nano: A New Era of Small Lasers

The impact of semiconductor lasers on our daily lives is immense. They perform work every time someone gathers information for the internet, makes a telephone call, prints an article or pays for an item at a store. There are over 2.5 billion VCSELs[†] in use at our homes or offices, and roughly 100 million are produced each year to keep up with demand. VCSEL technology is now considered conventional, and research has progressed to smaller devices, modulated at higher speeds and producing output with greater spectral stability. This chapter focuses on two of the advances. One is the reduction of optical cavity volume by as much as two orders of magnitude, making a transition from microlasers (such as VCSELs) to nanolasers. Two is a change in active medium from quantum wells (QWs) to quantum dots (QDs), bringing about, e.g., devices operating with very few (tens) of emitters. These developments ushered in a new era for semiconductor device physics, one where quantum optical and many-body electron interaction effects dominate. The underlying motivation is the control of spontaneous emission [1]. The typical laser mitigates the randomness (noise) caused by spontaneous emission by overwhelming it with stimulated emission. Here, we are speaking of actually quieting the spontaneous emission noise, both spatially and temporally. In the former, we use nanocavities to inhibit spontaneous emission in undesirable directions. With the latter, we

[†] Vertical cavity surface emitting lasers, cf. Chapter 34.

use very few QDs (ideally only one) to control the timing of photon emission, thereby improving photon statistics beyond the limit described by the Poisson distribution. Devices incorporating the two advances are being fabricated and experiments are being performed. The results are both promising and exciting from the device and physics aspects, respectively. They also lead to many new questions and renewed interest in some old ones: What is lasing and where is the threshold? Why is there not a phonon bottleneck? What is the homogeneous width of a QD transition [2–4]? What is the inhomogeneous broadening in my samples? Is there really thresholdless lasing [5–7]? Are QD lasers better than QW lasers [8]? Why do QD lasers not show modulation speeds as advertised? This chapter describes a theoretical framework capable of addressing all the abovementioned questions. The building blocks are come from quantum electrodynamics (QED), which is the quantum theory of the interaction of light with matter, and carrier interactions described in terms of many-body theory.

The fundamental concepts of lasing are often discussed in terms of rate equations for material excitations and cavity photons that may well be familiar to the reader. We begin this chapter with an excursion to show profit and limitations of laser rate equations for understanding the behavior of nanolasers, and at the same time establish a connection to more sophisticated semiconductor laser models. In Section 48.3, we give a short overview of the key aspects in modeling nanolasers and the characterization of their emission properties. In Section 48.4, we introduce a microscopic laser model for solid-state emitters that goes beyond the rate equations and that provides access to the quantum-statistical properties of the emission. A central aspect of device performance is determined by the efficiency of carrier scattering processes following excitation. Section 48.5 provides an overview of the underlying mechanisms of carrier–carrier and carrier-phonon interaction and explains methods to incorporate the dynamics into semiconductor laser models within different levels of approximation. The underlying formalism allows one to address a wide variety of effects present in semiconductor nanolasers, and we provide a few examples in Sections 48.6 and 48.7, where QD lasing and radiative coupling between individual emitters are discussed. Section 48.8 gives an outlook toward systems with only a few QDs inside the cavity, where the individual electronic many-particle properties of each emitter matter, and where device properties are dominated by quantum and correlation effects.

48.2 Connecting to Earlier Work: Laser Rate Equations and the β Factor

Lasing operation takes place when pumping of the active material provides sufficient gain to compensate the losses. It is thus determined by the interplay of the excitation and emission dynamics of the gain material, taking into account the feedback provided by the radiation field inside the resonator. A basic understanding of lasing action can be obtained from laser rate equations in the form of two coupled equations for the gain (in this case, the number of excitons N in the QD ensemble) and the intracavity photon number n:

$$\begin{aligned} \frac{\mathrm{d}}{\mathrm{d}t} N &= P - \gamma_l (n+1) N - \gamma_{\mathrm{nl}} N, \\ \frac{\mathrm{d}}{\mathrm{d}t} n &= -\kappa n + \gamma_l (n+1) N. \end{aligned} \tag{48.1}$$

Here, P and κ are the pump and photon loss rates, γ_l the spontaneous emission rate into the laser mode, γ_{nl} the rate of radiative recombination into other modes, and $\gamma_{\mathrm{sp}} = \gamma_l + \gamma_{\mathrm{nl}}$ the total spontaneous emission rate. The bracket $(n+1)$ contains both the stimulated and spontaneous emission contributions. The ratio

$$\beta = \frac{\gamma_l}{\gamma_{\mathrm{sp}}} \tag{48.2}$$

defines the β-factor illustrated in Figure 48.1. It is a key characteristic quantity of any laser device as it defines device performance in the spontaneous-emission regime (i.e., below threshold) and, more importantly, the threshold current. The rate equations (Equation 48.1) are often expressed in terms of β:

$$\begin{aligned}\frac{\mathrm{d}}{\mathrm{d}t}N &= P - \beta\gamma_{\mathrm{sp}}(n+1)N - (1-\beta)\gamma_{\mathrm{sp}}N,\\ \frac{\mathrm{d}}{\mathrm{d}t}n &= -\kappa n + \beta\gamma_{\mathrm{sp}}(n+1)N.\end{aligned} \tag{48.3}$$

In conventional lasers, $\beta \approx 10^{-5}$ [9], so that the majority of spontaneously emitted photons are lost. Once the system starts lasing at sufficiently high excitation, stimulated emission dominates over spontaneous emission, so that the fraction of photons lost into nonlasing modes becomes insignificant. This behavior can be directly traced by accessing both emission channels separately. In micropillar lasers, the fundamental mode often used as laser mode has a far-field emission in vertical direction of the pillar, whereas losses occur laterally through the pillar side walls. The input–output curve (photon number vs. pump rate) collected separately from both directions, together with a schematic of the experiment, is shown in Figure 48.2 [10]. As long as spontaneous emission is the dominating emission process, both emission intensities increase linearly with pump with a fixed ratio determined by the β factor. At higher excitation powers, stimulated emission from the laser mode sets in and photon emission from the laser mode increases nonlinearly and more strongly than the emission into loss channels. The resulting increase of the normalized ratio r of both emission channels therefore gives direct account of the onset of stimulated emission. Note that the S shape of the intensity curve for the lateral emission is due to stray light from the laser mode that is collected in lateral direction. Ideally, a clamped intensity is expected.

When continuous excitation is considered, the rate equations are solved in the steady state. Input–output curves obtained from the rate equations (Equations 48.1) for different values of β are shown in Figure 48.3. For $\beta \ll 1$, a sudden increase in emission intensity is visible that allows one to identify the lasing threshold. With increasing coupling efficiency β, the threshold shifts to lower pump rates, offering the prospect of devices with reduced threshold currents. At the same time, the intensity jump decreases until the "thresholdless" case is obtained for $\beta = 1$. In this regime an identification of the transition into lasing is impossible from the emission intensity alone. A characterization of the threshold requires going beyond the rate equation approximation to study statistical and coherence properties of the emission. One of the attractiveness of nanolasers is that they are capable of operating in a regime close to $\beta = 1$ due to their small effective mode volumes and large cavity lifetimes that cause strong funneling of spontaneously emitted photons into a single resonator mode [1]. At the same time, the photonic density of states is reduced away from the cavity-mode frequency, which further suppresses emission into nonlasing modes and thereby also

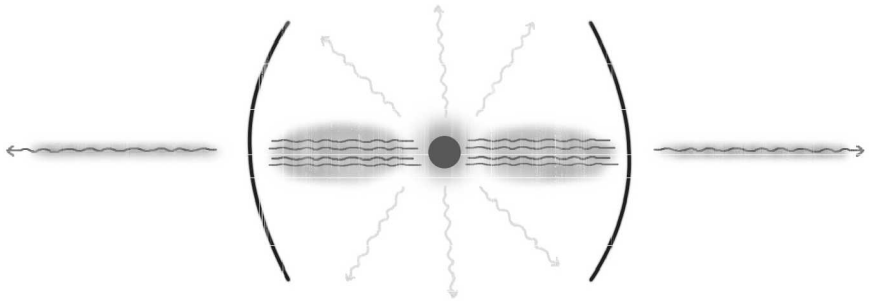

FIGURE 48.1 Spontaneous emission of the emitter into the laser mode (black lines) and into nonlasing modes (gray lines). The ratio of the spontaneous emission into the laser mode and the total spontaneous emission is described by the β factor.

9781498749565_C048 2017/8/5 7:29 Page 630 #4

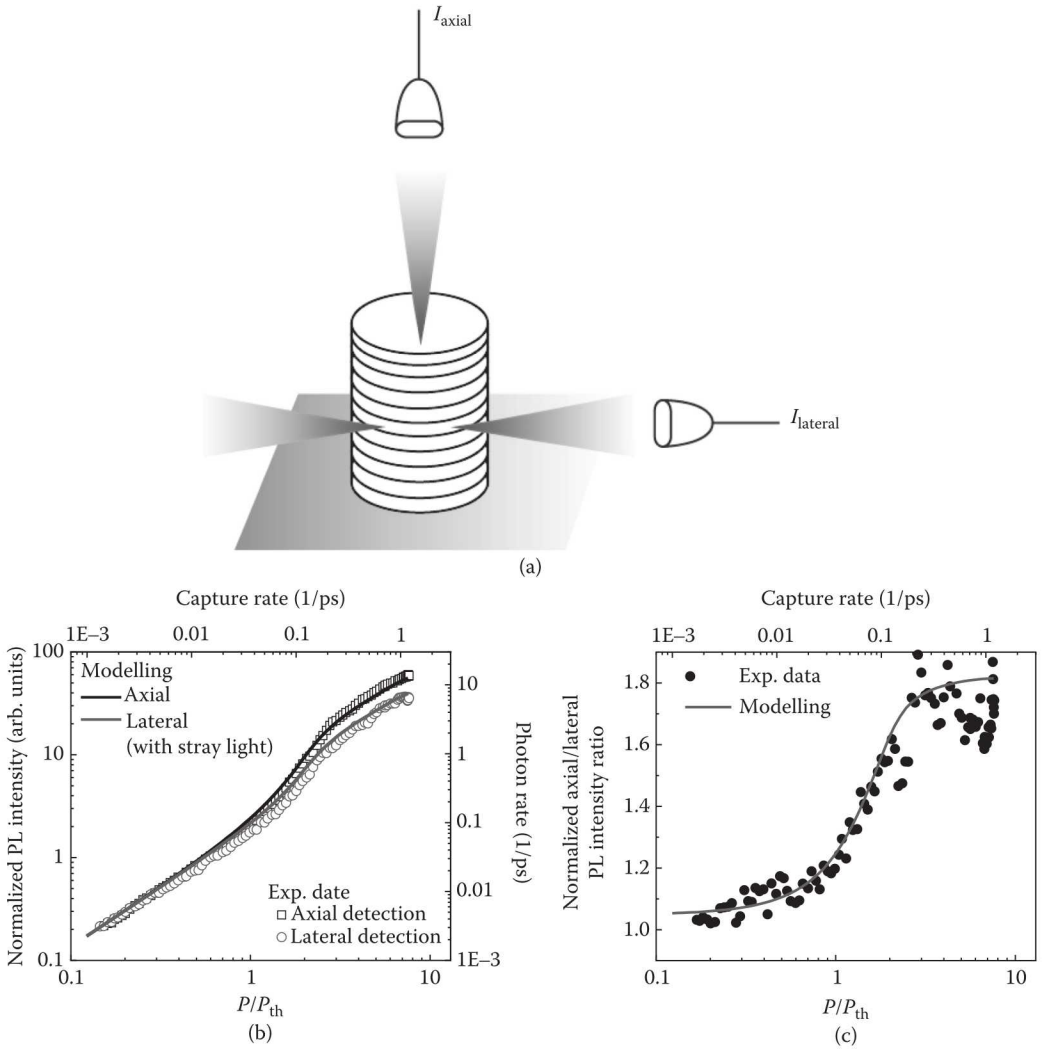

FIGURE 48.2 (a) Sketch of an experiment for detecting laser-mode emission in axial direction, and leaky mode emission in lateral direction separately. (b) Input–output characteristics of a quantum dot (QD) micropillar laser. Emission intensity into the laser mode (axial direction) and into nonlasing modes (lateral direction) are shown separately. (c) Their ratio r increases at the onset of stimulated emission, providing a direct visualization of the transition into the lasing regime. The results have been obtained from the semiconductor laser theory introduced in Section 48.4. Note that in lateral emission some scattered light from the axial emission is collected, which is responsible for the unclamped intensity behavior. [PL, photoluminescence. (Figures b and c adapted from Musiał, A. et al., *Physical Review B*, 91, 205310, 2015.)]

increases the β factor. While cavities operate at a specific narrow frequency window, structures that cause a broadband enhancement of spontaneous emission without using a cavity, such as photonic trumpets [11], are based on the very same concept.

The rate equations (Equation 48.1) have further drawbacks for modeling QD-based nanolasers. Most importantly, they do not provide information on laser field coherence and photon correlations. The rate equations are obtained by neglecting all correlations between light and matter degrees of freedom. Due to the enhanced interaction inside the microresonator, photon-, and carrier-photon correlations have been

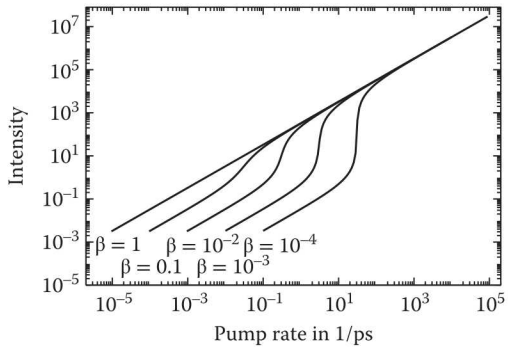

FIGURE 48.3 Laser input–output characteristics as obtained from rate equations. Shown are steady-state results at each pump value, parameterized by the β factor and the cavity loss rate. With increasing β, the threshold shifts to lower pumping and the laser threshold becomes increasingly hard to identify, and additional indicators beyond the reach of the rate-equation description are needed.

demonstrated to play an important role in nanolasers, and this is where new approaches are required to understand and control these properties for new devices. In Section 48.4, we introduce a systematic approach to include semiconductor and correlation effects in extended laser models and discuss effects in nanolasers that set these systems apart from conventional laser devices.

48.3 Key Aspects of Nanolasers

Nanolasers use resonators that confine light in a volume of the light wavelength cube or smaller. The free spectral range, i.e., the energetic distance between resonator modes, grows with decreasing size of the cavity mode volume. Consequently, there is increased potential that the material gain overlaps only with one, or at most, a very few modes [12] of the resonator, as illustrated in the top right panel of Figure 48.4. This sets them apart from other lasers, such as edge-emitting lasers and the typical VCSELs [13,14], where optical modes lie more densely and emission is typically multimode (left panel). A nano-resonator may be a disk or pillar, employing distributed-Bragg reflectors [15], total internal reflection at semiconductor-air interfaces [16], or photonic crystal cavities with defect sites [17].

It is a great advantage of small resonators that spontaneous emission enhancement $\propto Q/V$ can be used to strongly enhance the light–matter interaction and to favor emission into the single mode and thereby attain high values of the β factor that can approach unity. Here, V is the effective mode volume, and $Q = E/\Delta E$, with $E = \hbar\omega$ the mode energy, and ΔE the mode linewidth, is the quality factor of the mode. The spontaneous-emission enhancement is direly needed to make up for the limited amount of gain material that can be placed inside the cavity. This so-called Purcell enhancement [18] can be directly observed in the temporal decay of the emission signal following short excitation. This is shown in Figure 48.5 [19] for micropillar nanolasers of different diameter and, therefore, different effective mode volume V.

As mentioned in Section 48.2, additional indicators are required to identify lasing in high-β devices due to the vanishing kink in the input–output curve. The most established method is to identify the statistical fluctuations of the emitted light. In the thermal regime below threshold, photons prefer to come in bunches. Lasing, on the other hand, originates from a coherent state of the light field, and photons arrive randomly in time. A transition from bunching to close to Poissonian emission is therefore a strong indicator for crossing the threshold to lasing. State-of-the-art streak-camera measurements give a direct visual account of this behavior: Figure 48.6 [20] shows temporally resolved single photon detection events for a system that has been excited by a short laser pulse. Counting statistics can be used to identify single photons, photon pairs, or bunches of more photons as indicated by the boxes. In practice, measurements are repeated thousands

9781498749565_C048 2017/8/5 7:29 Page 632 #6

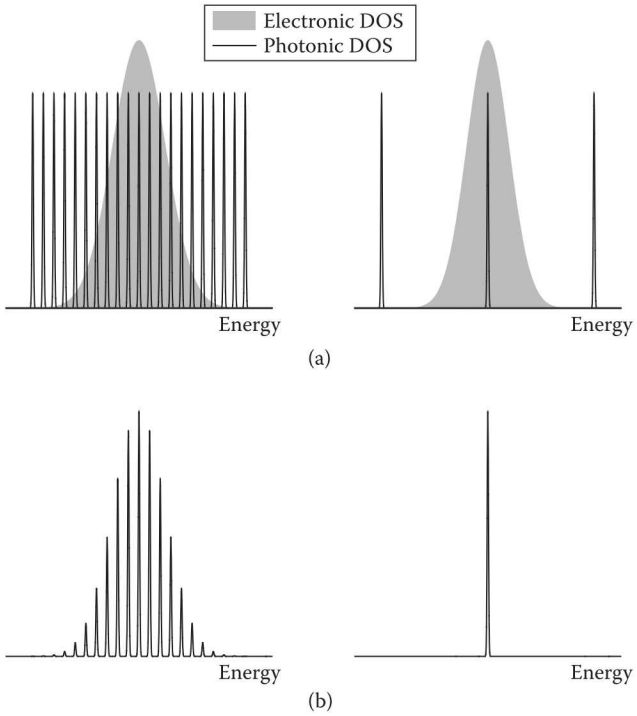

FIGURE 48.4 (a) Illustration of the photonic (black) and electronic (shaded) density of states of a typical laser (left) and a nanolaser (right) with the latter having a much larger free spectral range (energetic spacing between photon modes). The QD gain in the right panel is inhomogeneously broadened due to variations in composition or dimension, see Section 48.8. (b) The resulting spontaneous emission spectra are determined by the overlap of the photonic and electronic density of states. On the other hand, with the proper pillar, disk or photonic crystal design, a nanolaser can be single mode both below and above the lasing threshold. (DOS, density of states.)

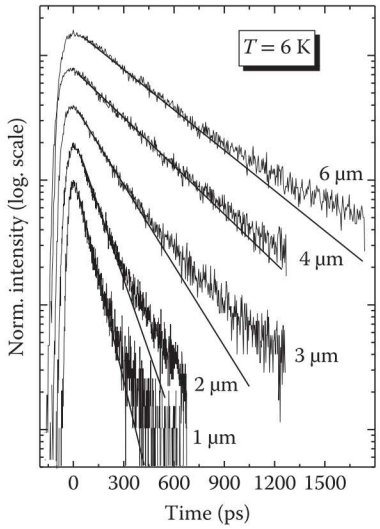

FIGURE 48.5 Time-resolved photoluminescence spectra following a *weak* excitation pulse. A decrease of the spontaneous emission time is observed with decreasing diameter of the micropillar cavities, reflecting the Purcell-enhancement $\propto Q/V$. The weak excitation ensures that the effect is not related to stimulated emission. (Reprinted from Schwab, M. et al., *Physical Review B*, 74, 045323, 2006. With permission.)

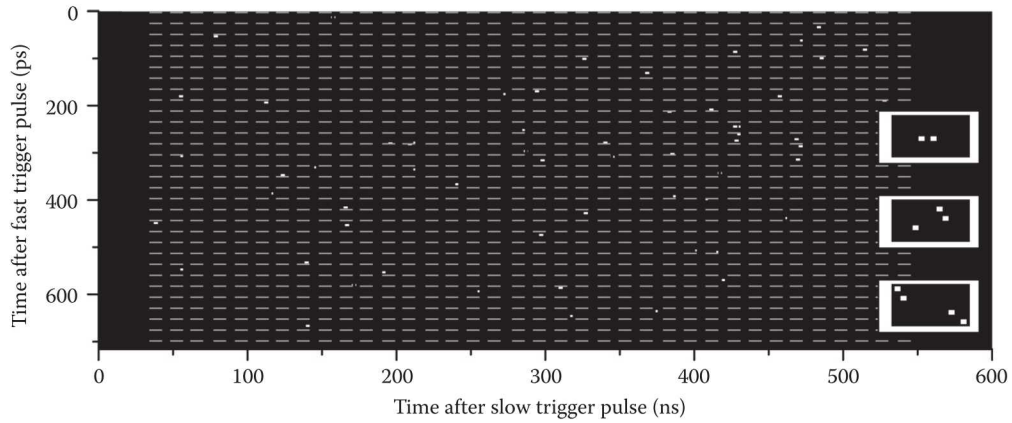

FIGURE 48.6 Streak-camera measurements provide impressive account of statistical fluctuations of the emitted light on the level of single photons. Single- and multiphoton emission events can be detected within a time-bin size of 2 ps (see magnification in the boxes) and provide insight into the quantum-mechanical state of the light field. To perform counting statistics in order to construct correlation functions like the ones shown in Figure 48.7, ten thousands of such measurements are performed. (Reprinted from Aßmann, M. et al., *Science* 325, 297–300, 2009. With permission).

of times. From the collected data, photon correlation functions $g^{(n)}$ can be obtained. They are of particular relevance, as they allow one to characterize the state of the quantum-mechanical light field as given by the distribution function p_n, which describes the *photon statistics* in terms of the probability of finding the system in the photon number state $|n\rangle$. Photon correlation functions are connected to the moments of the photon statistics:

$$\langle n^i \rangle = \sum_{k=0}^{\infty} k^i p_k. \tag{48.4}$$

As an example, the second-order photon-correlation function (sometimes referred to as photon autocorrelation function) is given by

$$g^{(2)} = \frac{\langle n^2 \rangle - \langle n \rangle}{\langle n \rangle^2}. \tag{48.5}$$

Correlation functions of order n take on a value of $n!$ if the light field is in a thermal state, and at all orders they possess a value of 1 for a perfectly coherent state [21]. For a micropillar QD nanolaser, this has been experimentally observed for $g^{(2)}, g^{(3)}$ and $g^{(4)}$ as function of pump rate, shown in Figure 48.7.

More commonly used than a streak camera is a Hanbury Brown and Twiss type measurement [22] schematically shown in Figure 48.8, where the bunching behavior of photons is quantified by the simultaneous registration of two photons at the two detector arms, providing access to the second-order correlation function $g^{(2)}$. For detectors, avalanche photodiodes (APDs) are used. Their time resolution is typically in the range of hundreds of picoseconds. Whether this resolution is sufficient depends on the type of measurement performed and the coherence time τ_{coh} of the emission signal. On the timescale of the latter, $g^{(2)}(\tau)$ goes to unity with respect to the delay time τ between two detection events, and the actual $g^{(2)}(0)$ at $\tau = 0$ can no longer be resolved if the detector's time resolution exceeds the coherence time, leading to the effect that $g^{(2)}(0)$ seems to take on a value of 1 even for thermal light [23].

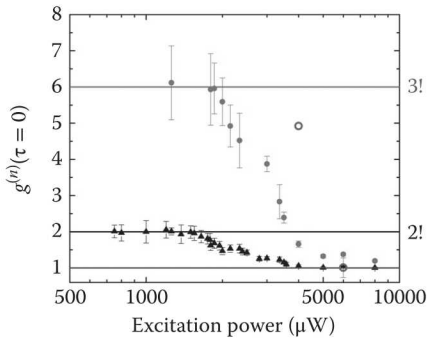

FIGURE 48.7 Photon autocorrelation functions $g^{(2)}(0)$ (triangles), $g^{(3)}(0)$ (dots), and $g^{(4)}(0)$ (open circles) as function of pump rate obtained from streak-camera measurements like the ones shown in the previous figure. For a typical LED to laser transition, all correlation functions show a transition from their thermal values $g^{(n)} = n!$ to that of a coherent field, $g^{(n)} = 1$. (Courtesy of Marc Aßmann, TU Dortmund.)

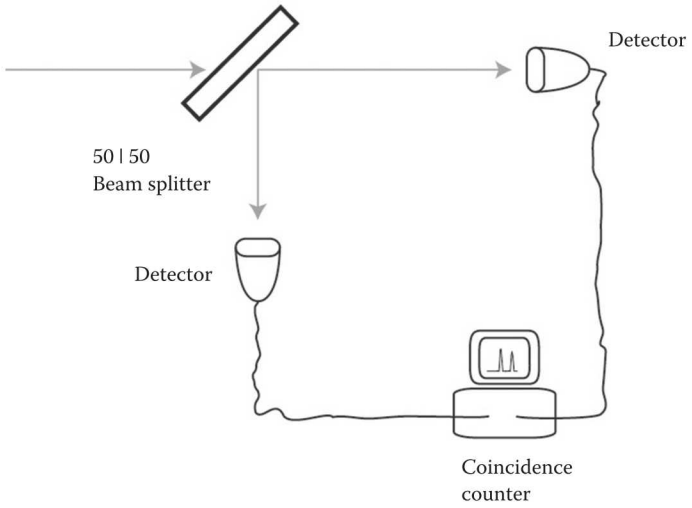

FIGURE 48.8 Illustration of a Hanbury Brown and Twiss measurement. A beam splitter distributes the emission between two detectors. Equal-time detection of two or more photons provides access to the second-order photon autocorrelation function $g^{(2)}(\tau = 0)$. A delay line in one arm can be used to measure $g^{(2)}(\tau \neq 0)$.

Another accessible indicator for coherent emission is a linewidth narrowing, or equivalently, an increase of the coherence time. Experimentally, the linewidth can be determined from spectra or Michelson interferometry measurements [21]. In the steady state $t = t_{ss}$, the coherence time τ_{coh} is related to the first-order coherence of the emission

$$\tau_{coh} = \int_{-\infty}^{\infty} d\tau \, |g^{(1)}(t_{ss}, \tau)|^2, \tag{48.6}$$

which requires the calculation of the two-time quantity in the integral by means of the quantum-regression theorem [24,25]. We will not go into more detail here and refer the reader to [26].

The criteria for lasing in nanolaser devices are a subject of much discussion [5,27]. Ideally, a combination of several criteria is used to identify the lasing regime and the threshold. These include the following:

1. Coherent emission approaching Poissonian photon statistics p_n.
2. A value close to 1 in the second-order photon correlation function $g^{(2)}(0)$. Note that this is a weaker criterion than i, as $g^{(2)}(0)$ is only linked to the first two moments of the full photon distribution function p_n, c.f. Equation 48.5.
3. An increase in the coherence time at the onset of lasing, when phase-coherent stimulated emission begins to dominate over spontaneous emission.
4. Cavity-photon-induced feedback of the gain material providing gain instead of absorption.
5. A mean intracavity photon number above 1.
6. An S-shaped nonlinear region in the input–output characteristics at threshold.
7. Carrier dynamics developing a hole-burning effect in the carrier-population functions at the energy of the laser transition, cf. Figure 48.13.

All of these criteria have their justifications, but on their own, neither may suffice to conclusively identify lasing. For example, coherent emission (1) is a prerequisite of lasing, but it may be realized without amplification (4 and 5) or originate from an external coherent drive. An S-shaped jump (6) in the input–output characteristic can originate from a variety of effects, such as a transition between multiexciton configurations feeding the laser mode [28], background contributions [29], or spectral wandering. On its own it is not a clear indicator for lasing. Moreover, lasing can take place in the absence of a nonlinear emission regime, e.g., if spontaneous emission losses are small ($\beta \to 1$), or saturation effects set in before the S shape can fully develop, which is particularly relevant under pulsed excitation [30].

48.4 Essential Physics I: Quantum-Optical Semiconductor Laser Theory

Different approaches can be taken in formulating a laser theory, including semiclassical methods, where the radiation field is classical and the system dynamics under the influence of the light–matter interaction is described by Maxwell–Bloch equations [31,32]. In the following, we introduce an extended laser model that accounts for semiconductor-specific effects, such as carrier scattering and dephasing, and that provides access to the statistical properties of the emission. The model is obtained in the framework of a correlation-expansion technique for the quantized light field interacting with carriers occupying the discrete QD conduction- and valence states. The method is versatile, as it allows one to include various aspects of semiconductor and correlation effects on a required level in a systematic and consistent manner. At the same time, the rate equations are contained as limiting case, as has been shown in [33].

In contrast to semiclassical approaches, using a quantized light field introduces the possibility to investigate emission properties beyond the classical regime. In fact, nonclassical effects, such as antibunched light emission around the threshold region, have been demonstrated in QD nanolasers [34]. In semiclassical models, the electromagnetic field drives a coherent polarization $\langle v_\nu^\dagger c_\nu \rangle$ across the bandgap of the semiconductor medium, as illustrated in Figure 48.9. The operators c_ν ($c_\nu^\dagger$) annihilate (create) a conduction-band carrier in the state $|\nu\rangle$, the operators v_ν ($v_\nu^\dagger$) are the equivalent for valence carriers. The resulting dynamics is familiar from atomic two-level models, where a resonant field drives Rabi oscillations. In a fully quantum-mechanical approach, the electromagnetic field is described by modes that are occupied by field quanta, the photons. If the modes are energetically well separated, like in a nanolaser, where the cavity possesses a large free spectral range, it suffices to consider the interaction of the active medium with photons in a single mode q. The coherent polarization $\langle v_\nu^\dagger c_\nu \rangle$ is then replaced by a photon-assisted polarization $\langle b_q^\dagger v_\nu^\dagger c_\nu \rangle$ that describes a carrier deexcitation (or excitation via $\langle b_q c_\nu^\dagger v_\nu \rangle$) by simultaneous emission (absorption)

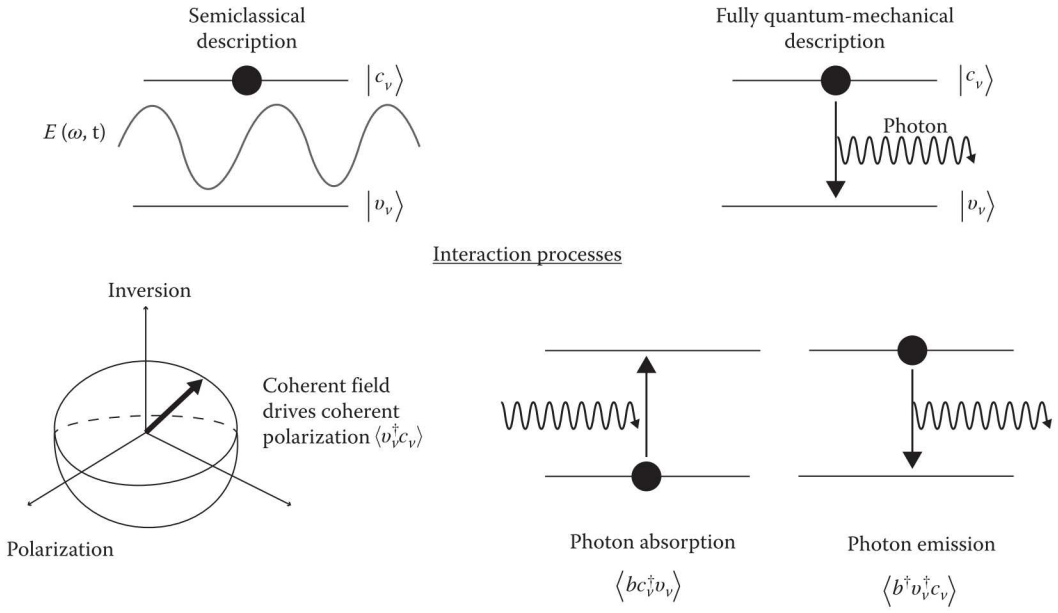

FIGURE 48.9 Illustration of the fundamental light–matter interaction in a semiclassical (left) and fully quantum-mechanical description (right). Semiclassically, matter degrees of freedom are described quantum-mechanically (e.g., by the states $|c_\nu\rangle$ and $|v_\nu\rangle$). The interaction with a classical coherent field $E(\omega, t)$ drives a coherent polarization $\langle v_\nu^\dagger c_\nu\rangle$. The polarization and population dynamics of often described in terms of the rotation of a vector on a unit sphere (Bloch sphere), as illustrated in the bottom left. By quantizing the light field, field quanta (photons) are introduced, and the fundamental interaction processes become the electronic (de)excitations via the simultaneous absorption or emission of a photon (bottom right). The semiclassical coherent polarization is replaced by the photon-assisted polarization $\langle b^\dagger v_\nu^\dagger c_\nu\rangle$.

of a photon into the mode q; the Bose operators b_q ($b_q^\dagger$) annihilate (create) a photon in mode q. The quantum-mechanical and semiclassical pictures are schematically compared in Figure 48.9.

The fully quantum-mechanical laser model is obtained by calculating the dynamical equations for carrier populations $f_\nu^c = \langle c_\nu^\dagger c_\nu\rangle$, $f_\nu^v = \langle v_\nu^\dagger v_\nu\rangle$ in the conduction and valence states of the QD, and the expectation value of the photon number operator in the laser mode q, for which we drop the index q in the following. These equations are obtained from Heisenberg's equations of motion for operators $A(t)$, $\dot{A} = i[H, A]/\hbar$. In the Hamiltonian, we consider the free contributions of QD single-particle states (first and second term in Equation 48.8) and the electromagnetic field (third term in Equation (48.8)), and the light–matter interaction,

$$H = H^{\text{free}} + H^{\text{LM}}, \tag{48.7}$$

with

$$H^{\text{free}} = \sum_\nu \varepsilon_\nu^c\, c_\nu^\dagger c_\nu + \sum_\nu \varepsilon_\nu^v\, v_\nu^\dagger v_\nu \; + \hbar\omega\left(b^\dagger b + \frac{1}{2}\right) \tag{48.8}$$

and

$$H_{\text{LM}} = -i\sum_{\alpha\nu}\left(g_{\alpha\nu}\, c_\alpha^\dagger v_\nu b + g_{\alpha\nu}\, v_\alpha^\dagger c_\nu b\right) + \text{h.c.} \tag{48.9}$$

Here, $\hbar\omega$ is the mode energy, and $g_{\alpha\nu}$ is the light–matter coupling strength that is determined by the overlap of the wave functions of the QD single-particle states $|\alpha\rangle$ and $|\beta\rangle$ and the mode function of the confined electromagnetic field [33]. The sums run over the single-particle states of the individual QD emitters, and the index is to be understood to contain both, QD label and single-particle state. The interaction Hamiltonian contains the elementary processes of electron–hole recombination and generation via emission and absorption of a photon, including the ones schematically shown in the bottom right of Figure 48.9.

48.4.1 Dynamical Laser Equations

For the dynamical evolution of the photon number $\langle b^\dagger b\rangle$ in the given mode and the electron and hole populations $f_\nu^e = \langle c_\nu^\dagger c_\nu\rangle$, $f_\nu^h = 1 - \langle v_\nu^\dagger v_\nu\rangle$, the contribution of the light–matter interaction H_{LM} in the Heisenberg equations of motion leads to [33]

$$\left(\hbar\frac{\mathrm{d}}{\mathrm{d}t} + \kappa\right)\langle b^\dagger b\rangle = 2\,\mathrm{Re}\sum_{\nu'}|g_{\nu'}|^2\,\langle b^\dagger v_{\nu'}^\dagger c_{\nu'}\rangle, \tag{48.10}$$

$$\hbar\frac{\mathrm{d}}{\mathrm{d}t}f_\nu^{e,h} = -2\,\mathrm{Re}\,|g_\nu|^2\,\langle b^\dagger v_\nu^\dagger c_\nu\rangle. \tag{48.11}$$

Here, we have scaled $\langle b^\dagger v_\nu^\dagger c_\nu\rangle \to g_{q\nu}\,\langle b^\dagger v_\nu^\dagger c_\nu\rangle$ to have the modulus of the coupling matrix elements appear. The finite lifetime of the cavity mode is introduced by considering a complex mode energy, $\tilde{\omega} = \omega - i\kappa$, where κ is directly connected to the Q-factor of the laser mode, $Q = \hbar\omega/2\kappa$. The dynamics of the photon number is determined by the abovementioned photon-assisted polarization $\langle b^\dagger v_\nu^\dagger c_\nu\rangle$ that describes the expectation value for a correlated event, where a photon in the mode q is created in connection with an interband transition of an electron from a conduction to a valence state. The sum over ν involves all possible interband transitions from various QDs.

An important component of the carrier dynamics is the recombination into nonlasing modes giving rise to the β factor discussed in Section 48.2. For the fraction $1-\beta$ of carriers emitting into nonlasing modes, a term proportional to the spontaneous emission rate can be added to the carrier population equations to account for the losses [33]:

$$\frac{\mathrm{d}}{\mathrm{d}t}f_\nu^{e,h}\Big|_{\mathrm{nl}} = \gamma_{\mathrm{sp}}(1-\beta)f_\nu^e f_\nu^h. \tag{48.12}$$

In contrast to the rate equations (Equation 48.3), the spontaneous emission losses in a semiconductor are determined by both electron and hole populations. The dynamical equation for the cavity-photon-assisted polarization is given by

$$\left(\hbar\frac{\mathrm{d}}{\mathrm{d}t} + \kappa + \Gamma + i\left(\tilde{\varepsilon}_\nu^e + \tilde{\varepsilon}_\nu^h - \hbar\omega\right)\right)\langle b^\dagger v_\nu^\dagger c_\nu\rangle =$$
$$f_\nu^e f_\nu^h - \left(1 - f_\nu^e - f_\nu^h\right)\langle b^\dagger b\rangle + \frac{1}{g_\nu}\sum_\alpha g_\alpha C^{\mathrm{x}}_{\alpha\nu\nu\alpha} + \delta\langle b^\dagger b c_\nu^\dagger c_\nu\rangle - \delta\langle b^\dagger b v_\nu^\dagger v_\nu\rangle. \tag{48.13}$$

The free evolution of $\langle b^\dagger v_\nu^\dagger c_\nu\rangle$ is determined by the detuning of the QD transitions from the cavity laser mode. This oscillatory term drops out if the transition is in perfect resonance with the mode. Only accounting for identical resonant QDs is a common and well-justified practice in ensembles of many (>100 emitters), as the summation over all QDs becomes a mere prefactor of the QD number, which is a significant simplification. In a semiconductor, the source term of spontaneous emission is described by an expectation value of four carrier operators $\langle c_\alpha^\dagger v_\alpha v_\nu^\dagger c_\nu\rangle$, see [35]. The Hartree–Fock factorization of this source term

leads to $f_\nu^e f_\nu^h$, which appears as the first term on the right hand side of Equation 48.13. Corrections to this factorization are included in $C^{\mathrm{x}}_{\alpha'\nu\nu'\alpha} = \delta\langle c^\dagger_{\alpha'} v^\dagger_\nu c_{\nu'} v_\alpha\rangle$. Dephasing is what destroys a coherent polarization. In semiconductors, dephasing arises from carrier scattering processes, excitation of carriers, and from the interaction with lattice vibrations that are responsible for the homogeneous linewidth. These contributions are here summarized in a phenomenological constant Γ.

The correlation functions $\delta\langle b^\dagger_q b_q c^\dagger_\nu c_\nu\rangle$ and $\delta\langle b^\dagger_q b_q v^\dagger_\nu v_\nu\rangle$ introduce carrier-photon correlations that are neglected on the level of rate equations. Their time evolution is given by [33]

$$\left(\hbar\frac{\mathrm{d}}{\mathrm{d}t} + 2\kappa\right)\delta\langle b^\dagger b c^\dagger_\nu c_\nu\rangle = -2\left|g_\nu\right|^2 \mathrm{Re}\Big[\delta\langle b^\dagger b^\dagger b v^\dagger_\nu c_\nu\rangle + \left(\langle b^\dagger b\rangle + f^e_\nu\right)\langle b^\dagger v^\dagger_\nu c_\nu\rangle\Big], \tag{48.14}$$

$$\left(\hbar\frac{\mathrm{d}}{\mathrm{d}t} + 2\kappa\right)\delta\langle b^\dagger b v^\dagger_\nu v_\nu\rangle = 2\left|g_\nu\right|^2 \mathrm{Re}\Big[\delta\langle b^\dagger b^\dagger b v^\dagger_\nu c_\nu\rangle - +\left(\langle b^\dagger b\rangle + f^h_\nu\right)\langle b^\dagger v^\dagger_\nu c_\nu\rangle\Big] \tag{48.15}$$

which couples to

$$\left(\hbar\frac{\mathrm{d}}{\mathrm{d}t} + 3\kappa + \Gamma + i\left(\tilde{\varepsilon}^e_\nu + \tilde{\varepsilon}^h_\nu - \hbar\omega\right)\right)\delta\langle b^\dagger b^\dagger b v^\dagger_\nu c_\nu\rangle = -2\left|g_\nu\right|^2\langle b^\dagger v^\dagger_\nu c_\nu\rangle^2 + 2\Big[\langle b^\dagger b\rangle + f^h_\nu - f^e_\nu\Big]\times$$
$$\Big[\delta\langle b^\dagger b c^\dagger_\nu c_\nu\rangle - \delta\langle b^\dagger b v^\dagger_\nu v_\nu\rangle\Big] - (1 - f^e_\nu - f^h_\nu)\,\delta\langle b^\dagger b^\dagger b b\rangle \tag{48.16}$$

and

$$\left(\hbar\frac{\mathrm{d}}{\mathrm{d}t} + 4\kappa\right)\delta\langle b^\dagger b^\dagger b b\rangle = 4\left|g_\nu\right|^2 \sum_{\nu'}\delta\langle b^\dagger b^\dagger b v^\dagger_{\nu'} c_{\nu'}\rangle. \tag{48.17}$$

On this level of approximation, we obtain a closed system of coupled equations that go beyond the rate equations by containing carrier-photon and photon–photon correlation functions that provide access to the second-order photon-correlation function

$$g^{(2)}(\tau = 0) = 2 + \frac{\delta\langle b^\dagger b^\dagger b b\rangle}{\langle b^\dagger b\rangle^2}. \tag{48.18}$$

48.4.2 Pump Process for Continuous-Wave-Excited Lasers

The earlier equations describe the light–matter interaction of a semiconductor system in terms of carrier populations and the polarization-analogue for the quantized light field, i.e., the photon-assisted polarization. An important component is yet missing, namely the interaction of charge carriers with the environment that allows for some sort of excitation mechanism. Pumping can be either done by current injection or by optical excitation. In both cases, electrons and holes are typically created in the continuum states of the wetting layer (WL) or barrier material, from where they are captured into the discrete QD states. This incoherent capture is one example of carrier scattering processes that, at this stage, are still missing from our description. While the quantitative modeling of these many-body processes is discussed in detail in Section 48.5, for continuous-wave (CW) excitation it is often sufficient to consider only the dynamics of carriers in the localized QD states. In its most simple form, two localized states are used for electrons and holes each, which closely resembles a four-level laser scheme. This choice is physically motivated by the electronic structure of typical QDs, which, depending on their size, consist of several confined states. We refer to the lowest (highest) and second-lowest (second highest) electron (hole) state as *s*- and *p*-states, respectively, as shown in Figure 48.10. In this reduced level scheme, the *p*-states are used for carrier pumping at rate P, which approximates the combined effect of carrier excitation in higher

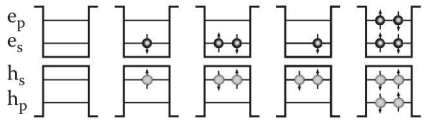

FIGURE 48.10 In a QD with several confined single-particle states for electrons and holes (the s- and p-states are shown), a multitude of many-particle configurations can be realized by occupying these states with electrons and holes. These many-particle configurations contain the neutral, charged, and multiexciton states, and dark states that differ in energy due to the Coulomb interaction between carriers.

states and the successive capture into the QD states:

$$\frac{\mathrm{d}}{\mathrm{d}t} f_{\mathrm{p}}^{\mathrm{e}}\Big|_{\mathrm{Pump}} = P(1 - f_{\mathrm{p}}^{\mathrm{e}} - f_{\mathrm{p}}^{\mathrm{h}}) \tag{48.19}$$

$$\frac{\mathrm{d}}{\mathrm{d}t} f_{\mathrm{p}}^{\mathrm{h}}\Big|_{\mathrm{Pump}} = P(1 - f_{p}^{\mathrm{e}} - f_{\mathrm{p}}^{\mathrm{h}}). \tag{48.20}$$

The blocking factors in the brackets ensure that the occupation remains bounded by unity. From their generation in the QD *p*-states, a phenomenological set of equations distributes carriers into the QD s-states:

$$\frac{\mathrm{d}}{\mathrm{d}t} f_{\mathrm{s}}^{\mathrm{e}}\Big|_{\mathrm{scatt}} = \gamma_{\mathrm{p}\to\mathrm{s}}^{r,e} f_{\mathrm{p}}^{\mathrm{e}}(1 - f_{\mathrm{s}}^{\mathrm{e}}) - \gamma_{s\to p}^{r,e} f_{\mathrm{s}}^{\mathrm{e}}(1 - f_{\mathrm{p}}^{\mathrm{e}}) \tag{48.21}$$

$$\frac{\mathrm{d}}{\mathrm{d}t} f_{\mathrm{s}}^{\mathrm{h}}\Big|_{\mathrm{scatt}} = \gamma_{\mathrm{p}\to\mathrm{s}}^{r,h} f_{\mathrm{p}}^{\mathrm{h}}(1 - f_{\mathrm{s}}^{\mathrm{h}}) - \gamma_{s\to p}^{r,h} f_{\mathrm{s}}^{\mathrm{h}}(1 - f_{\mathrm{p}}^{\mathrm{h}}) \tag{48.22}$$

$$\frac{\mathrm{d}}{\mathrm{d}t} f_{\mathrm{p}}^{\mathrm{e}}\Big|_{\mathrm{scatt}} = -\gamma_{\mathrm{p}\to\mathrm{s}}^{\mathrm{r,e}} f_{\mathrm{p}}^{\mathrm{e}}(1 - f_{\mathrm{s}}^{\mathrm{e}}) + \gamma_{s\to p}^{\mathrm{r,e}} f_{\mathrm{s}}^{\mathrm{e}}(1 - f_{\mathrm{p}}^{\mathrm{e}}) \tag{48.23}$$

$$\frac{\mathrm{d}}{\mathrm{d}t} f_{\mathrm{p}}^{\mathrm{h}}\Big|_{\mathrm{scatt}} = -\gamma_{\mathrm{p}\to\mathrm{s}}^{\mathrm{r,h}} f_{\mathrm{p}}^{\mathrm{h}}(1 - f_{\mathrm{s}}^{\mathrm{h}}) + \gamma_{\mathrm{s}\to\mathrm{p}}^{\mathrm{r,h}} f_{\mathrm{s}}^{\mathrm{h}}(1 - f_{\mathrm{p}}^{\mathrm{h}}). \tag{48.24}$$

Equations 48.21 through 48.24 are motivated in the more general concepts of carrier kinetics in the following section. Together, Equations 48.10–48.24 serve as an accessible and complete model for QD-based lasers, and we discuss exemplary results in Section 48.6.

48.5 Essential Physics II: Carrier Kinetics in QD Systems

As we overviewed in Section 48.2, rate equations can provide important insights for the theoretical understanding of lasers. They can be used to describe input–output curves [36–39], and, combined with Langevin approaches [40,41] even the photon statistics and intensity noise.

An important reason why carrier dynamics is essential for the understanding of laser operation is the excitation mechanism. To see this, let us assume that carrier populations in lasers are given by Fermi–Dirac distribution functions (often a reasonable approximation). This implies that states with below-average kinetic energy are Pauli-blocked for the excitation mechanism. This is illustrated in Figure 48.11, where states with above-average kinetic energy (shaded in green) are available for the excitation, while states with below-average kinetic energy (shaded in red) are not. Therefore, it is important to understand how carriers, injected at the green-shaded area, end up in the spectral window from where they recombine. Accountable for this are two mechanisms that we discuss in this section. The carrier–carrier Coulomb interaction redistributes carriers between different states and leads to an equilibration towards a Fermi–Dirac distribution [42–46]. But as every carrier scattered downward in energy is partnered by a scattering partner that is scattered upward (right sketch in Figure 48.12), the Coulomb scattering is not able to dissipate energy.

9781498749565_C048 2017/8/5 7:29 Page 640 #14

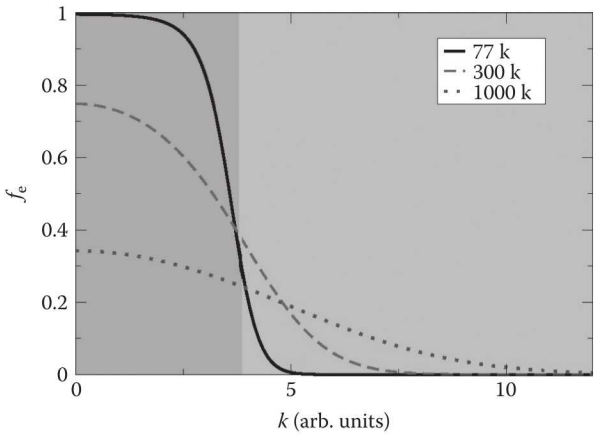

FIGURE 48.11 Fermi–Dirac distribution for electrons in a QW at different temperatures and a carrier density of $5 \times 10^{11}\text{cm}^{-2}$, the shading background indicates the availability for carrier injection for the low-T distributions.

FIGURE 48.12 Conceptual sketch of carrier scattering processes. Left: carrier–phonon interaction, right: carrier–carrier Coulomb interaction.

This leads to a hot Fermi–Dirac function such as depicted in Figure 48.11, that has significantly different properties regarding inversion and gain. The cooling toward the lattice temperature is provided by the carrier-phonon interaction [47–51], that provides for the cooling by taking up the energy of the hot carriers and distributing it toward crystal lattice (left sketch in Figure 48.12). In a laser under CW-excitation conditions the energetic difference from excitation to emission energy also leads to heating and often the carrier-phonon interaction is not strong enough to provide complete cooling towards the lattice temperature. Therefore, a dynamical equilibrium is reached that may consist of Fermi–Dirac distributions with several 100K above the lattice temperature [52,53].

As already outlined in Section 48.4, it is generally necessary to set up equations of motion not for the total carrier density N but for individual carrier populations of different single particle states $f_\alpha^c = \langle c_\alpha^\dagger c_\alpha \rangle$ to describe these effects. Such so-called "kinetic equations" together with the laser equations, Equations 48.10 through 48.20, enable us to treat excitation kinetics and turn-on dynamics of semiconductor QD-based laser systems and will be the topic of this section.

The question of what timescales and by which processes the carriers approach (quasi-) equilibrium conditions (if at all) influences the design of laser devices, as the answer to these questions determines, e.g., the dynamical response and turn-on delay [53–57]. While rate equations can also describe the turn-on dynamics for conventional laser devices, where carrier dynamics takes place on a fs to ps timescale, whereas the laser turn-on happens on the order of 10 ns, the situation is very much different in nanocavities with large Purcell enhancement, i.e., the enhancement of the spontaneous emission rate due to the presence of the cavity, where the turn-on delay can be on the order of 10 ps [53,58] and thus on the same timescale as the carrier scattering. The use of population function both for QD and WL states also allows one to describe effects such as spectral hole burning, or the difference between optical and injection pumping, that are unavailable to a theoretical model that tracks only the dynamics of the total carrier density N.

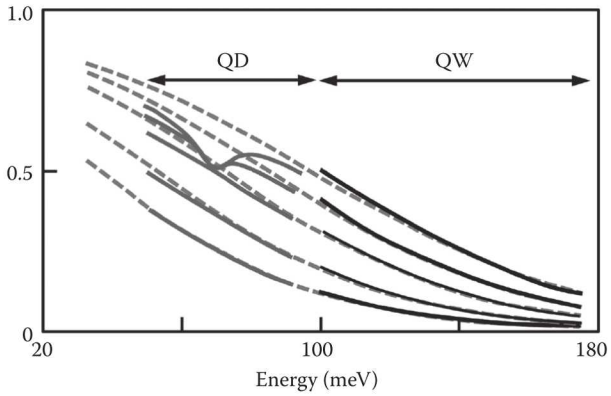

FIGURE 48.13 Carrier populations in a QD+WL system under laser operation for increasing pump intensity. The blue lines describe the population of QD carriers (subject to inhomogeneous broadening), the black lines show the populations of the WL states. For high pump rates the "hole" burnt into the population function by laser operation is clearly visible. The shaded-dashed lines are corresponding Fermi–Dirac functions. (From Chow, W. W. et al., *Light: Science & Applications*, 3, e201, 2014. With permission.)

An example of such carrier population functions are shown in Figure 48.13. The seemingly continuous features of the discrete QD single-particle state populations originate from the large number of emitters in the inhomogeneously broadened ensemble, cf. Section 48.8.

The simplest equation for such state-dependent carrier dynamics is given by

$$\frac{\mathrm{d}}{\mathrm{d}t}f_\alpha = (1-f_\alpha)\Gamma_\alpha^{\mathrm{in}} - f_\alpha\Gamma_\alpha^{\mathrm{out}}, \tag{48.25}$$

where $\Gamma_\alpha^{\mathrm{in}}$ and $\Gamma_\alpha^{\mathrm{out}}$ give the in- (out-) scattering rates into (out of) the state α. A more detailed version of Eq. (48.25) has the structure

$$\frac{\mathrm{d}}{\mathrm{d}t}f_\alpha = \sum_\beta f_\beta(1-f_\alpha)\gamma_{\beta\to\alpha} - f_\alpha(1-f_\beta)\gamma_{\alpha\to\beta} \tag{48.26}$$

and describes that the population of state α is enlarged by scattering from β to α and reduced by scattering from α to β. The Pauli-blocking terms $f_\beta(1-f_\alpha)$ and $f_\alpha(1-f_\beta)$ occur as scattering has to be proportional to the occupancy f of the initial and to the non-occupancy $(1-f)$ of the final state. Under continuous excitation (CW laser), it may suffice to restrict the description to the s-shell and p-shell states of the QD and to use phenomenological scattering rates $\gamma_{\beta\to\alpha}^{e,h}$, in which case we recover Equation 48.21 through 48.24 in Section 48.4.

An often used approximation that is generally of relevance if not only QD states are discussed but also the continuous states of the WL or barrier are taken into consideration is the so-called relaxation time approximation

$$\frac{d}{dt}f_\alpha = \frac{f_\alpha - F_\alpha(N,T)}{\tau}, \tag{48.27}$$

which describes the relaxation of a nonequilibrium carrier population f_α toward a Fermi function $F_\alpha(N,T)$ at temperature T and carrier density N on a time-scale τ. While this approximation often works well, it also necessitates to determine the time-scale τ and the carrier temperature T. The last point is not trivial as in laser devices the carriers typically posses a higher temperature than the lattice [52,53]. To answer these

questions and also to investigate situations where the relaxation time approximation (Equation 48.27) is not applicable we have to take the microscopic origin of the scattering process into account. In the following, we discuss the dominant physical mechanisms behind the carrier dynamics, which are carrier-phonon scattering and carrier–carrier Coulomb scattering.

48.5.1 Carrier–Phonon Interaction

As discussed earlier, carrier temperature is an important factor for laser operation as it controls the population inversion. Hence the optical gain depends strongly on the temperature of the carrier system [59,60]. As the carrier–carrier Coulomb interaction cannot dissipate energy, the source for thermalization of the carriers toward the lattice temperature is the interaction with phonons. To investigate this interaction mechanism, we first have to determine which phonon modes are responsible for the carrier dynamics. A main difference between different phonon branches is whether they are longitudinal or transversal in nature. One can show [61] that due to their ability to form polarizations, mainly longitudinal phonons couple to the carrier system and that for most situations the interaction with transversal phonons is negligible. This leaves us with two phonon branches that are most important for the carrier-phonon interaction. These are the longitudinal optical (LO) phonons and longitudinal acoustic (LA) phonons. The speed of propagation of an acoustic phonon, which is also the speed of sound in the lattice, is given by the slope of the acoustic dispersion relation, $\frac{\partial \omega_k}{\partial k}$. At low values of k, the dispersion relation is almost linear, and the speed of sound is approximately independent of the phonon wavenumber.

Even though we are interested in laser structures, where the active material is composed of nanostructures (QDs), it is a good approximation to take the phonon modes and interaction potentials of the surrounding bulk material. This is the case, as we are mostly interested in long-wavelength phonons where the phonon wavelength is much larger than the size of the nanostructure we are investigating.

The interaction of carriers with LO phonons can be described by the Fröhlich coupling [61]. As this coupling mechanism is Coulombic in nature, the corresponding interaction matrix elements drop off rapidly with increasing momentum transfer $\mathbf{q}$. Therefore a often used approximation consists of treating the LO phonons as dispersionless with constant frequency $\hbar\omega_{\mathbf{q}} = \hbar\omega_{\mathrm{LO}}$ [62]. For acoustic phonons, the main interaction mechanisms are the deformation potential coupling and the piezoelectric coupling [62]. While these play an important role in the line broadening of QD lines in the low temperature and low carrier-density regime, they do not provide an efficient source for carrier scattering.

The interaction matrix elements for the interaction of carriers with LO-phonons are [60,63]

$$|M_{\alpha\beta}|^2 = \frac{M_{\mathrm{LO}}^2}{e^2/\varepsilon_0} V_{\alpha\beta\alpha\beta}, \tag{48.28}$$

containing Coulomb matrix elements $V_{\alpha\beta\alpha\beta}$ (see Equation 48.33 and Reference [64]), the elementary charge e and the vacuum permittivity ε_0. The prefactor $M_{\mathrm{LO}} = 4\pi\alpha\frac{\hbar}{\sqrt{2m}}(\hbar\omega_{\mathrm{LO}})^{\frac{3}{2}}$ includes the polar coupling strength α and the reduced mass m. The matrix elements are given here in a way that explicitly shows the Coulombic nature of the carrier-LO-phonon coupling.

A first approach toward carrier scattering is given by the Boltzmann equation [40,61]. For carrier-phonon scattering, this is given by Equation 48.26 with

$$\gamma_{\beta\to\alpha} = \sum_q M_{\beta\alpha}(q)\Big((1+n_q)\delta(\epsilon_\beta - \epsilon_\alpha - \hbar\omega_{\mathrm{LO}}) + n_q\delta(\epsilon_\beta - \epsilon_\alpha + \hbar\omega_{\mathrm{LO}})\Big). \tag{48.29}$$

The terms proportional to n_q and $(1 + n_q)$ describe phonon absorption and emission processes. In QD systems, additional effects exist that are not described within the framework of a Boltzmann equation, but are closely connected to carrier scattering, as they stem from the same microscopic interaction mechanism. These are quasi-particles and non-Markovian effects. The main reason is that the carrier-phonon interaction leads to the formation of a new quasi-particle. The quasi-particle obtained by dressing the carriers with the carrier-phonon interaction—the polaron—describes the lattice distortion accompanying the electron in its motion. In the framework of Green's functions (GFs), polarons are described using the retarded GF Kadanoff–Baym equation [63]:

$$\left[i\hbar\frac{\partial}{\partial\tau} - e_\alpha^a\right] G_\alpha^{a,R}(\tau) = \delta(\tau) + \int d\tau' \;\Sigma_\alpha^{a,R}(\tau-\tau')\, G_\alpha^{a,R}(\tau'). \tag{48.30}$$

The corresponding retarded selfenergy in random-phase approximation (RPA) [62] is given by

$$\Sigma_\alpha^{a,R}(\tau) \;=\; i\hbar \sum_\beta \;|M_{\alpha\beta}|^2 G_\beta^{a,R}(\tau)\, d^<(-\tau), \tag{48.31}$$

where the phonon propagators $d^{\gtrless}$ contain the phonon frequency and the phonon population [63]. The spectral function $\hat{G}_\alpha(\hbar\omega) = 2\mathrm{Im}(G_\alpha^{a,R}(\hbar\omega))$, which follows from the retarded GF, can be seen as a generalization of the single particle energy, i.e., a free particle has a spectral function of the form $\hat{G}_\alpha(\hbar\omega) = \delta(\epsilon_\alpha - \hbar\omega)$. In contrast, the Polaronic spectral functions but also posses a finite spectral width that is connected to the lifetime of the respective quasi-particle.

Using the quasi-particles as described by the polaron retarded GF, we can formulate a quantum-kinetic equation for polaron scattering:

$$\frac{\partial f_\alpha^a(t)}{\partial t} = 2\,\mathrm{Re}\sum_\beta \int_{-\infty}^{t} dt'\; |M_{\alpha\beta}|^2 G_\beta^{a,R}(t,t')\left[G_\alpha^{a,R}(t,t')\right]^* \\ * \;\left\{\left[f_\beta^a(t')(1-f_\alpha^a(t'))\right] d^>(t',t) - \left[f_\alpha^a(t')(1-f_\beta^a(t'))\right] d^<(t',t)\right\}, \tag{48.32}$$

which contains scattering by phonon emission and absorption processes just as in the Boltzmann equation. Effects included here that go beyond the Boltzmann treatment are a weakening of the exact energy conservation due to the polaron properties (finite spectral width) and due to non-Markovian effects described by the explicit dependence of the time change of f_α^a at time t on all earlier times.

Results from such a quantum-kinetic treatment are shown in Figure 48.14. The QD level spacing is chosen to be 10% higher than the LO-phonon energy of 36meV. Therefore, a Boltzmann scattering equation predicts a complete inhibition of scattering due to the δ-functions in Equation (48.29). In contrast, the quantum-kinetic treatment shows that, due to quasi-particle effects (dotted line), scattering channels open up. The solid line shows the combined influence of quasi-particles and non-Markovian effects, that are caused by the time integrals in Equation (48.32). The inhibition of scattering as given by a Boltzmann equation, was predicted as a "phonon-bottleneck" early on [65,66], however, fast-carrier scattering was observed e.g., in Reference [67], showing the relevance of polaronic effects. For details see References [63,68,69].

48.5.2 Coulomb Interaction

The most important carrier scattering mechanism in the regime of high excitation densities, relevant for laser operation, is the carrier–carrier Coulomb interaction. It leads to a fast redistribution of carriers from

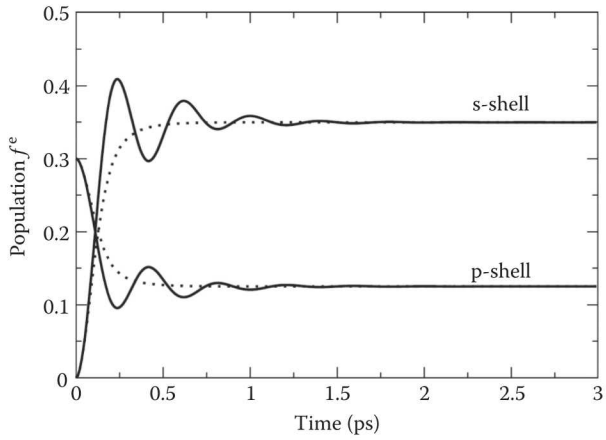

FIGURE 48.14 Redistribution of carrier occupations due to scattering of electrons from p-shell to s-shell in a QD via the carrier phonon interaction. In a Boltzmann-equation approach the occupations would remain constant due to a complete lack of scattering processes as described in the text (Reprinted from Seebeck, J. et al., *Physical Review B*, 71, 125327, 2005. With permission).

the spectral window where excitation takes place toward the spectral window from where they recombine. While Coulomb scattering cannot dissipate energy and thermalize the system (see Figure 48.12), it leads to equilibration toward a hot Fermi–Dirac function.

To determine the strength of the Coulomb interaction in nanostructures, we need to determine Matrix elements of the Coulomb interaction in the single-particle basis given by, e.g., tight-binding descriptions of QDs. Using such single-particle wavefunctions, we can construct the Coulomb matrix elements

$$V_{\alpha\beta\gamma\delta} = \frac{1}{A} \sum_{\mathbf{q}} V_{\mathbf{q}} \left\langle \alpha \left| e^{-i\mathbf{q}\cdot\mathbf{r}} \right| \delta \right\rangle \left\langle \beta \left| e^{+i\mathbf{q}\cdot\mathbf{r}} \right| \gamma \right\rangle, \tag{48.33}$$

consisting of overlap integrals between single-particle wavefunctions and the Coulomb potential $V_{\mathbf{q}}$ [64]. A closer analysis of these Matrix elements also points towards a source for the efficiency of Coulomb scattering in nanostructures. Even though the available phase space of scattering partners is reduced significantly in QDs, compared to QW or bulk systems, this is partially balanced by enhanced interaction matrix elements due to the strong localization of the QD wave functions.

Like for the carrier-phonon scattering a first description of carrier–carrier scattering can be given by a Boltzmann-type equation

$$\begin{aligned} \frac{\mathrm{d}}{\mathrm{d}t} f_\alpha(t) = & \frac{2\pi}{\hbar} \sum_{\beta\gamma\delta} \left(\left| W_{\alpha\gamma\delta\beta} \right|^2 - W_{\alpha\gamma\delta\beta} W^*_{\alpha\gamma\beta\delta} \right) \delta(\epsilon_\alpha - \epsilon_\beta + \epsilon_\gamma - \epsilon_\delta) \\ & \Big[f_\beta(t)(1 - f_\alpha(t)) f_\delta(t)(1 - f_\gamma(t)) - f_\alpha(t)(1 - f_\beta(t)) f_\gamma(t)(1 - f_\delta(t)) \Big], \end{aligned} \tag{48.34}$$

which contains screened interaction matrix elements $W_{\alpha\gamma\delta\beta}$ and an energy conserving δ-function. A feature of the carrier–carrier Coulomb scattering in QDs is that, while most scattering channels become extremely inefficient at low carrier density due to the population factors in Equation (48.34), some some scattering channels like electron–hole scattering are possible at very low carrier densities [70].

Results for the carrier–carrier Coulomb scattering in a QD laser under optical CW excitation are presented in Figure 48.15, where the carrier population functions is shown as a function of energy for different times. discrete symbols denote the QD populations for s-shell and p-shell and the lines the continuous

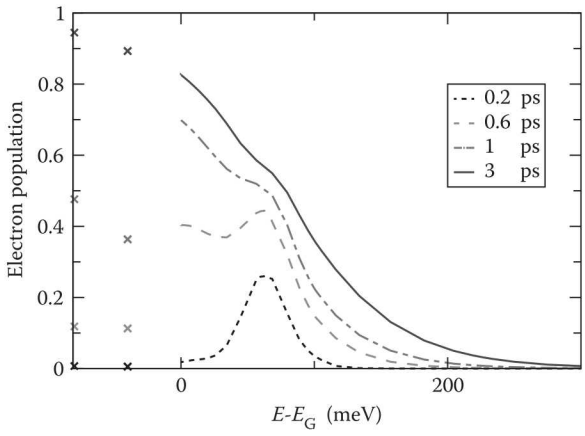

FIGURE 48.15 Carrier populations as a function of energy for electrons in a QD system under laser operation for different times. Symbols denote QD populations, lines WL populations. (Reprinted from Lorke, M. *Applied Physics Letters*, 99, 151110, 2011. With permission.)

WL states that are optically excited. After the initial Gaussian population profile has been excited by the pump, an ultra-fast redistribution is observed, that immediately starts to populate the QD states. It should be noted that, contrary to an often assumed situation [56,71], the timescales between the relaxation dynamics in the WL and the dynamics of the QD populations are not decoupled. On one hand, this is due to the efficiency of the initial in-scattering into the QD, as the QD states are initially empty. On the other hand, the relaxation within the WL is significantly slower than in a pure QW, as the capture into the QD states is most efficient for the WL states with low quasi-momenta. Therefore, these states are constantly depleted during the early stage of the kinetics, which slows down the relaxation of the WL distribution itself toward a quasi-equilibrium distribution [53] Furthermore, after the initial relaxation that lasts about 3 ps, a heating of the carrier population is observed on a timescale of 100 ps, as the pumping into the WL injects carriers at a higher energy than the emission energy.

These results also show (compared to those of the preceding section) that Coulomb and phonon scattering act on the same timescale in QD systems.

As for the phonons, quantum-kinetic effects lead to quasi-particle formation and non-Markovian effects. The corresponding quantum-kinetic equations can be written as

$$\frac{\partial f_\alpha^a(t)}{\partial t} = \frac{2}{\hbar}\mathrm{Re}\sum_{\beta\gamma\delta}\int_{-\infty}^{t} \mathrm{d}t'\Big(\left|W_{\alpha\gamma\delta\beta}\right|^2 - W_{\alpha\gamma\delta\beta}W^*_{\alpha\gamma\beta\delta}\Big)G_\beta^{a,\mathrm{R}}(t,t')\left[G_\alpha^{a,\mathrm{R}}(t,t')\right]^* * G_\delta^{a,\mathrm{R}}(t,t')\left[G_\gamma^{a,\mathrm{R}}(t,t')\right]^*$$
$$* \Big[f_\beta(t')(1-f_\alpha(t'))f_\delta(t')(1-f_\gamma(t')) - f_\alpha(t')(1-f_\beta(t'))f_\gamma(t')(1-f_\delta(t'))\Big]. \quad (48.35)$$

As for the Boltzmann-type equation for carrier scattering, this equation contains direct and exchange scattering, proportional to $\left|W_{\alpha\gamma\delta\beta}\right|^2$ and $W_{\alpha\gamma\delta\beta}W^*_{\alpha\gamma\beta\delta}$, respectively. The energy conserving δ-function is generalized by the product of retarded GFs just as for the carrier-phonon interaction and via the explicit time dependence on earlier times memory effects are included. While these equations have not been evaluated in detail due to their numerical complexity, it is expected that the included quasi-particle and non-Markovian effects would influence several properties of nanolasers. On one hand, large signal modulation and turn-on delay are expected to be influenced by non-Markovian effects. On the other hand, quasi-particle effects can, as for the carrier-phonon interaction, alter the scattering rates

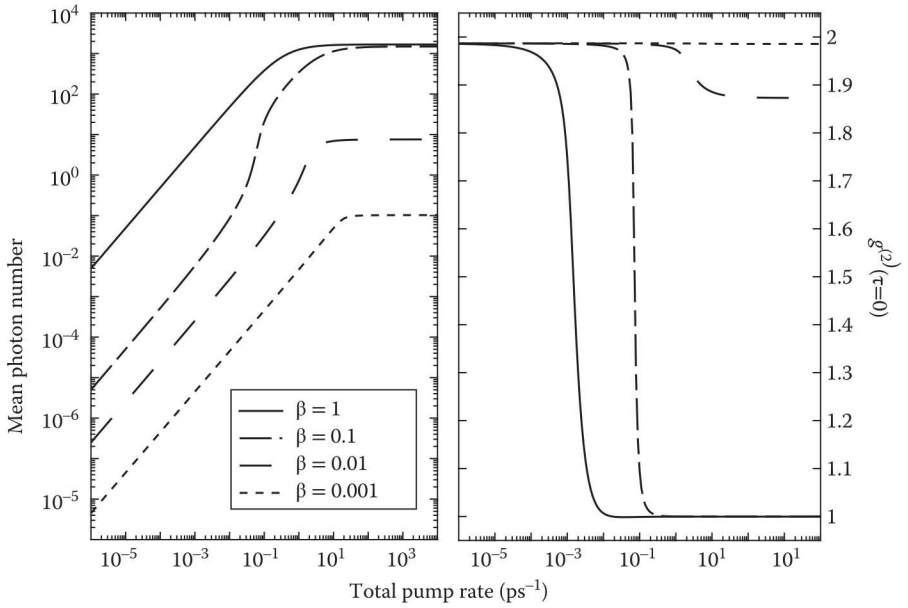

FIGURE 48.16 Input–output curves (left) and autocorrelation function $g^{(2)}(0)$ (right) for a nanolaser with 300 QD emitters. Curves are shown for different values of the β factor. For $\beta = 1$, a visible threshold is absent in the input–output curve, whereas $g^{(2)}(0)$ shows a clear transition from thermal to coherent emission. Note that the jump from below to above threshold is larger than in the results obtained from rate equations (Figure 48.3) and does here no longer scale with $1/\beta$. For $\beta = 0.1$, a soft kink appears in the input–output curve. For smaller values of β, the limited number of QD emitters cannot provide sufficient gain to reach lasing before saturation is reached. A cavity-Q factor of 32,000 and a cavity-enhanced spontaneous emission rate of $\tau_{sp} = 50$ ps has been used.

influencing also the modulation response and threshold current. In the photon-assisted polarization, Equation 48.13 exist analogous expressions to the scattering contributions given in Equation 48.35 that lead to excitation-enhanced dephasing

$$\frac{\mathrm{d}}{\mathrm{d}t}\langle b^\dagger \nu_\alpha^\dagger c_\alpha\rangle(t) = \int_{-\infty}^{t} \mathrm{d}t'(-\Gamma_\alpha^{\mathrm{DD}}(t,t'))\langle b^\dagger \nu_\alpha^\dagger c_\alpha\rangle(t') + \sum_\beta \Gamma_{\alpha\beta}^{\mathrm{OD}}(t,t')\langle b^\dagger \nu_\beta^\dagger c_\beta\rangle(t'), \tag{48.36}$$

where Γ^{DD} and Γ^{OD} consist of interaction matrix elements W, retarded GFs $G^{a,\mathrm{R}}$ and population functions f_α in a similar way as they appear in Equation 48.35 for the carrier scattering. We have investigated the influence of quasi-particle and non-Markovian effects on the quasi-classical analogues of these quantities in detail to study optical gain spectra of QD systems [8,60,72–75] and we expect an influence of these contributions to the turn-on behavior and the modulation dynamics [38].

48.6 Connecting to Experiments: Transition to Lasing and the β Factor

As first example, we discuss characteristic input–output curves and statistical properties of a Purcell-enhanced QD nanolaser device. In Figure 48.16 results from the semiconductor laser model are shown for various values of the β factor and fixed number of QD emitters. For $\beta = 1$, all spontaneous emission is

directed into the laser mode. In contrast to the rate-equation result that we have discussed in the context of Figure 48.3, saturation is visible at strong pumping. This effect is important in QD nanolasers, since the small size of the resonator naturally limits the amount of gain material that can be brought into the cavity. A monotonous increase of the output intensity with pumping, as given by the rate equations (Equation 48.1), would be unphysical. As a consequence, for smaller values of β, the gain can become insufficient to reach lasing before saturation sets in. In the example in Figure 48.16, this is visible for $\beta = 0.01$, where the threshold is reached, but the emission remains largely thermal with $g^{(2)}(0) \approx 1.9$, and for $\beta = 0.001$, where the QD emission saturates long before the laser threshold at a low mean intracavity photon number of 0.1. Access to the photon autocorrelation function $g^{(2)}(0)$ provides an important tool in judging the emission properties far beyond what can be inferred from the emission intensity alone and is a significant advancement over the rate equations.

Deeper insight into cavity-QED effects in nanolasers can be obtained from the emission and correlation *dynamics*. The left panel in Figure 48.17 shows time resolved the emission pulse (solid curves) and autocorrelation function $g^{(2)}(t, \tau = 0)$ (symbols) following picosecond-short optical excitation of the nanolaser. Also here the high time resolution has been realized by using a streak-camera setup. Following a sufficiently strong excitation pulse, the statistical properties of the emission pulse change as function of time from thermal to coherent and back to thermal. Coherent emission is reached around the peak region of the emission pulse and forms a plateau when the excitation level is above the threshold region. The data agrees well with time-dependent results of the laser model (right panel), which are readily available from the time evolution of the coupled differential equations presented in Section 48.4. In contrast to conventional measurements that integrate over the emission pulse, here it is possible to track the degree of coherence during the pulse and to provide an understanding of the coherence it contains. In their combination, state-of-the art measurements and microscopic models can reveal new aspects of solid-state light sources, reflecting the emission dynamics and the dynamics of quantum-mechanical correlations down to the few-photon level. The explicit treatment of dynamical properties of nanolasers, such as carrier dynamics, turn-on delay, and modulation response requires to go beyond the simple approach in Equations 48.21 through 48.24 for the carrier scattering and use the more involved methods of Section 48.5 due to the sensitivity of these quantities [55].

48.7 Interemitter Coupling Effects and Superradiance in Nanolasers

When several emitters couple to a common light field, the interaction introduces correlations between them. The eigenstates of the interacting system are then no longer given by those of the individual systems, but by so-called Dicke states of the collective system. In 1954, Dicke has shown [76] that from certain collective states, emission can be enhanced or suppressed, which is referred to as superradiance and subradiance. In particular, for the Dicke state of the half inverted system of N two-level emitters, the recombination rate is proportional to $N(N-1)$ [77]. This quadratic behavior with emitter number has become one of the hallmarks of superradiance. Since its discovery by Dicke, superradiance has been extensively and continuously studied in a variety of systems. Most commonly, however, superradiance is associated with temporal modifications of the emission in spatially extended systems, such as clouds of atoms [78] or, when it comes to semiconductor systems, excitons in extended systems [79].

In an ensemble of QDs that are embedded in a microcavity, depending on the inhomogeneous broadening of the QDs and the cavity Q factor, a fraction of the QDs overlaps both spectrally and spatially with the mode. The common light field these resonant solid-state emitters are subjected to provides a mechanism to form inter-emitter correlations that can lead to sub- and superradiant effects in QD nanolasers. Laser models typically assume that emitters act individually and neglect such effects. In the following, we outline how to use the formalism introduced in Section 48.4 to formulate a laser theory that includes inter-emitter coupling in an approximative way and give a quantitative discussion of its effects. As it turns out, their

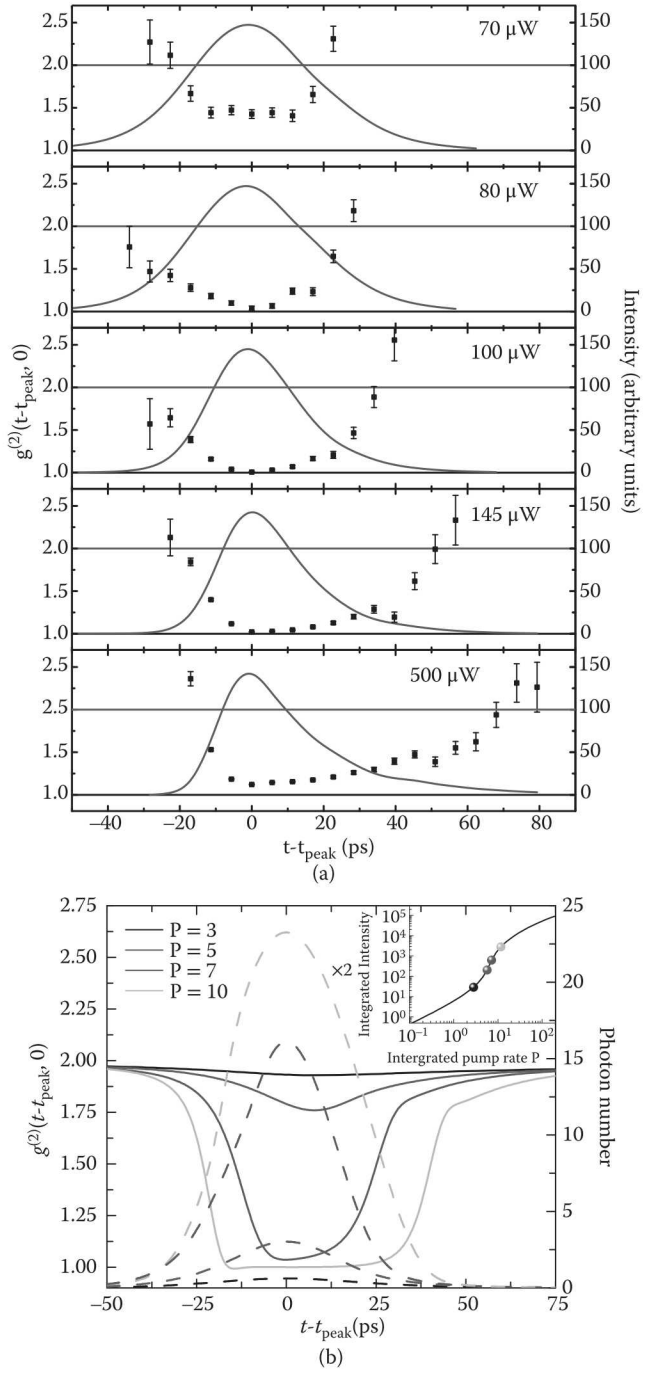

FIGURE 48.17 Time-resolved measurements (a) and theoretical results (b) for emission intensity and photon autocorrelation function following picos-second short optical excitation of a QD-micropillar laser. (Reprinted from Aßmann, M. et al., *Physical Review B* 81, 165314, 2010. With permission).

impact on both stationary and dynamical laser properties can be quite significant. A detailed description of the formalism is found in [80].

To this end, we introduce a formulation for operators that act on the electronic QD states in terms of the many-particle configurations $|i\rangle$, where i refers to configurations like ground state, exciton, trion, biexciton, various dark states, etc. These configuration states, some of which are shown in Figure 48.10, form the basis of the single-QD subspaces of the Hilbert space. Operators Q_{ij}^{α} are introduced that describe either transitions from configuration j to configuration i for $i \neq j$, or the probability that configuration i is realized for $i = j$ in QD α. This approach has advantages over descriptions that use single-particle operators c_ν and v_ν, like we did in Section 48.4. In doing so, many-electron configurations of one emitter are addressed by a single operator Q rather than many single-particle creation and annihilation operators. It further simplifies the systematic approximation scheme used to truncate the hierarchy of equations of motion with respect to correlations involving *different* QDs. Interemitter correlations are described by a hierarchy of expectation values $\langle Q_{ij}^{\alpha} Q_{kl}^{\beta} \rangle$, $\langle Q_{ij}^{\alpha} Q_{kl}^{\beta} Q_{mn}^{\gamma} \rangle$, … that involve transitions in QDs α and β, or QDs α, β and γ, etc. The cluster expansion approach facilitates a truncation at a certain order of interemitter coupling, e.g. on the level of pair-correlations between emitters given by $\langle Q_{ij}^{\alpha} Q_{kl}^{\beta} \rangle$ and illustrated in Figure 48.18. All quantum-mechanical expectation values containing electronic QD operators acting on more than two emitters are then neglected. On this level, which is the lowest order that contains interemitter coupling effects, a system of N identical QDs with four confined states each is described by about 300 coupled differential equations, also including photon correlations up to the fourth order providing access to the autocorrelation function $g^{(2)}(0)$. The generation of the equations of motion can be assisted by using computer algebra [80]. While the formalism may appear to involve a great deal of effort, it is highly efficient in the numerical evaluation, and computations for many emitters can typically be performed on a single workstation.

The impact of interemitter coupling on the steady-state properties of a continuously driven QD nanolaser can be seen in Figure 48.19. In the top panel, input–output curves are shown that have been obtained from two separate calculations, one including and one omitting QD–QD correlations. C_F in the bottom panel visualizes the difference in the output intensity I, i.e.,

$$C_F = \frac{I_{\text{rad. coupled QDs}}}{I_{\text{independent QDs}}} - 1. \tag{48.37}$$

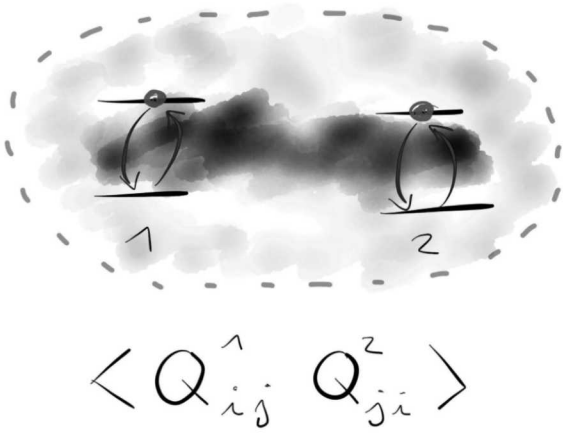

FIGURE 48.18 Illustration of photon-mediated inter-emitter dipole correlations between two emitters.

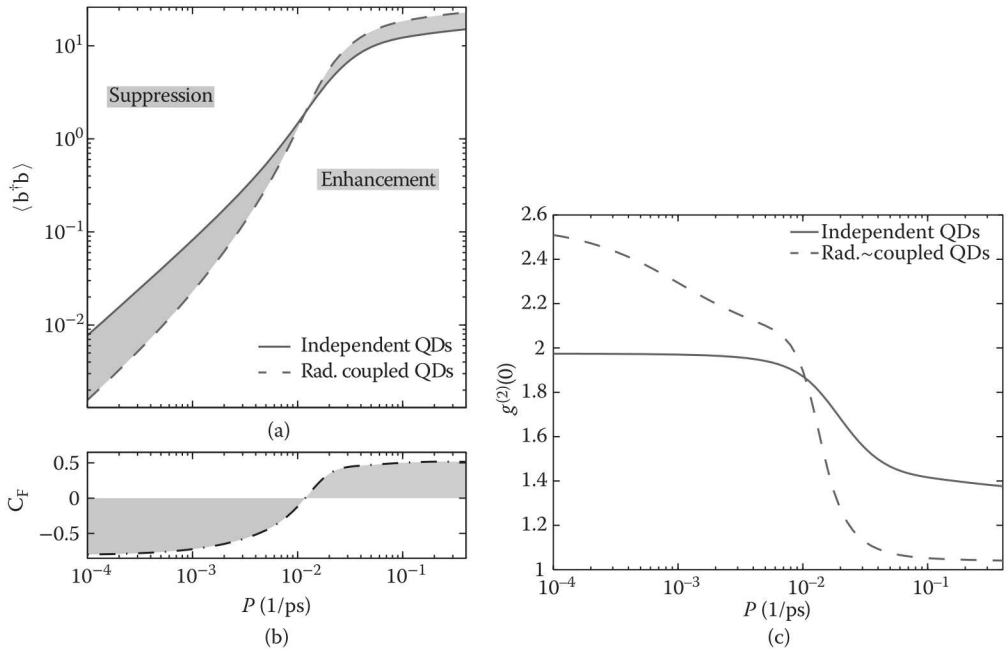

FIGURE 48.19 (a) Input–output curve for a QD nanolaser with typical specifications: 100 resonant emitters, cavity loss rate $\kappa = 0.05/\text{ps}$ (corresponding to $Q = 20,000$), carrier relaxation rate $\gamma_r = 0.05/\text{ps}$, and spontaneous losses into leaky modes $\gamma_{spont} = 0.01/\text{ps}$. (b) The cooperativity factor visualizes the difference caused by the radiative coupling. (Adapted from Leymann, H. A. M. et al., *Physical Review Applied*, 4, 044018, 2015. With permission.) (c) Corresponding autocorrelation functions. At low excitation, superthermal bunching is a signature of the subradiant emission regime. At high excitation, the threshold to lasing is not fully crossed if emitters act individually and radiative coupling is neglected. Dipole–dipole correlations between distant emitters create additional coherence in the superradiant regime.

The possibility to "switch" the coupling on an off is a particular advantage of the equation-of-motion method and allows to directly assess the impact of the radiative coupling. The following effects are observed:

1. In the low-excitation regime, the inter–emitter coupling creates a subradiant state with a reduced spontaneous emission rate and reduced photon output. Once the laser threshold is crossed, a superradiant state is formed which enhances the laser output *in addition* to stimulated emission provided by photons in the cavity. In sum, the effect on the input–output curve over the whole excitation regime is quite significant. In particular, in the given example, which has been calculated for a typical microcavity laser with 100 QD emitters as active medium, one would underestimate the true β factor by one order of magnitude when ignoring the radiative coupling
2. The input/output characteristics exhibit a different and untypical slope below threshold.
3. In the subradiant regime (low emission intensity), dipole correlations between pairs of QDs cause an increased probability to emit photons synchronously, leading to super-thermal bunching behavior in the statistical properties of the emission, as shown in the right panel of Figure 48.19.
4. Due to inter-emitter coupling, fewer QDs are required to reach the lasing threshold. In small systems, where achieving sufficient gain due to the limited number of emitters in the cavity has always been an issue, the presence of radiative coupling can explain why lasing is more easily reached than expected from conventional laser theories that do not include QD–QD correlations.

5. Coherent emission with $g^{(2)}(0) = 1$ is achieved at lower intracavity mean photon number in the presence of interemitter coupling. This may be interpreted as an increase in the "coherence per photon" due to the alignment of dipole correlations between emitters.

Interestingly, these theoretical predictions are hard to verify experimentally. A strong indicator for the presence of a dipole-correlated phase is the super-thermal photon bunching [81], which has recently been observed in time-resolved studies using a streak-camera setup in combination with microscopic theory [82]. In the same study, highly accelerated spontaneous emission and subradiant photon trapping have been demonstrated. In their sum, the observation of these criteria give a convincing account of the presence of strong inter-emitter coupling effects in a typical QD nanolaser.

48.8 Nonresonant Coupling and Lasing from Multiexciton States in Few-QD Systems

An inherent property of self-assembled QDs that are grown in the so-called *Stranski-Krastanov* mode [83] is inhomogeneous broadening. It refers to inhomogeneity in size, shape and material composition from one QD to the next, causing differences in the confinement potential and with it the electronic single-particle states. While the typical linewidth of QD transitions is tens to hundreds of μeV depending on temperature [2,84,85], the line of an ensemble of self-assembled QDs consists of the spectral lines of the individual emitters, which for many emitters then appears as a single line with a typical broadening of 20–50 meV. An illustrative demonstration of this behavior is given in Figure 48.20 [86]. Inhomogeneous broadening is generally seen as a weak point of self-assembled QDs, as it takes away some of the advantage of the narrow and well-defined transition energies that is characteristic for the single emitter. On the other hand, in cavity-QED it simplifies the task of creating spectral overlap between emitters and a cavity mode (cf. Figure 48.4) and compensates for spectral wandering, since the ensemble broadening is large compared to the cavity linewidth (typically 50–500 μeV). The influence of detuning of emitters in the ensemble and a cavity mode is greatly reduced by nonresonant coupling mechanisms discussed later. The influence of inhomogeneous broadening on QD laser properties has been studied in the framework of a QD laser theory in [27].

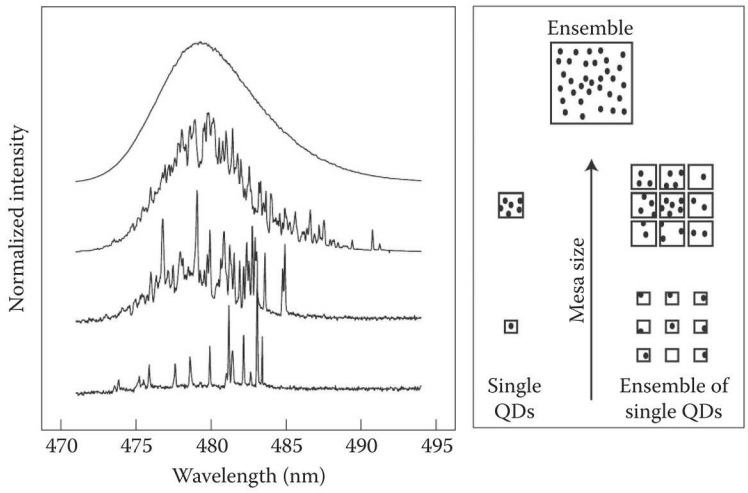

FIGURE 48.20 Experimental results illustrating inhomogeneous broadening in a quantum dot (QD) ensemble. With decreasing mesa size, the QD ensemble consists of fewer and fewer emitters (illustrated right). The broad inhomogenous emission spectrum for many emitters (top left) is revealed to consist of discrete lines as the number of emitters is reduced (bottom left). (Reprinted from Scheibner, M. et al., *Nature Physics*, 3, 106–110, 2007. With permission.)

In this section, we look into what happens if the resonator contains only a few emitters, and the gain spectrum consists of a multitude of separate sharp lines. Such a situation is depicted in the left panel of Figure 48.21. Then, the emission properties are determined by the interplay of various many-particle configurations of each QD emitter, and their contribution to the photon production depends on the relative spectral position to the cavity mode. While at first it seems contradictory that lasing can be achieved in such a system, strong emission enhancement can drive even a single emitter close to the regime of lasing. At the same time, nonresonant coupling mechanisms haven been identified to provide means for a detuned QD to emit photons into the cavity mode. Nonresonant cavity feeding plays a significant role in nanolasers with ensembles of emitters, but a quantification of its effect is nearly impossible to obtain in such a system. The few-emitter limit, however, offers the unique possibility to study non-resonant mode coupling in a highly controllable environment. In fact, the underlying physical process has long been elusive. Intensive research on this topic has identified three mechanisms that are responsible for the effect:

1. Accoustic phonons can bridge small energy gaps in the range of 1 meV between a detuned emitter resonance and the cavity mode [87–92]. The efficiency is determined by the imbalance between phonon-assisted cavity-photon emission, and the reverse process. Low temperature favors this asymmetry, because low phonon population makes the emission of a phonon more likely than its absorption. Therefore, phonon-mediated nonresonant coupling is more efficient for coupling blue-detuned emitter transitions to the mode [93].
2. At higher carrier densities, interactions with the quasi-continuous WL states provide means for Auger-like scattering processes that allow to bridge larger energy gaps of up to 10 meV [94–98]. While their efficiency is small in comparison to the ultrafast intraband relaxation [53,64,99–101], Auger-coupling is of central importance in the high-excitation regime of nanolasers.
3. QDs possess a rich electronic structure that gives rise to a multitude of multiexciton states, as illustrated in Figure 48.10. The Coulomb interaction energetically separates transitions from different multi-exciton states. This energetic separation, and the possibility of interband recombinations from higher confined states (e.g., the p shell) covers an even larger energetic window, as has been shown

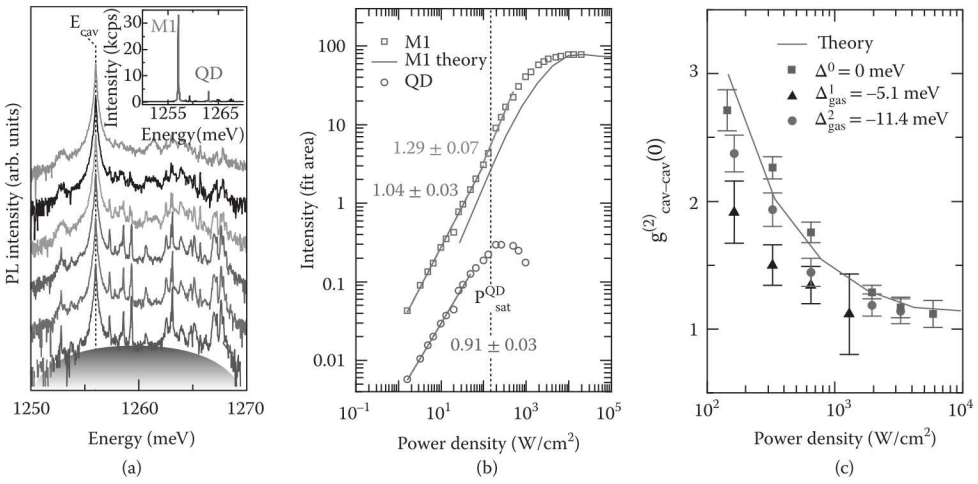

FIGURE 48.21 **(a)** Spectra of a few-quantum dot (QD) photonic-crystal cavity laser for excitation energies ranging from 0.14 to 5.9 kW/cm^2. **(b)** Input–output curves at the cavity-mode energy (squares) and the QD exciton (circles), the latter showing saturation while the cavity-mode emission continues to increase. **(c)** Second-order photon correlation function at the cavity mode for three different detunings of the cavity-mode energy. Irrespective of the detuning between QD transitions and mode, lasing is achieved at sufficiently high excitation. [PL, photoluminescence. (Reprinted from Lichtmannecker, S. et al., 2016, February. A few-emitter solid-state multi-exciton laser. *ArXiv:1602.03998 [condmat]*).]

in [98,102,103]. Thus, even if the QD exciton line, which dominates the spectrum at low excitation, is detuned from the cavity mode, a higher transition, e.g., from the biexciton, may be in perfect resonance with the mode and lead to efficient photon production at higher excitation.

There are several approaches to include the non-resonant coupling of detuned emitters in a laser theory, which superficially all have the same effect of producing additional photons in the resonator mode. In their origin they differ fundamentally, which is reflected in the saturation behavior and in the statistical properties of the emission. On the one hand, a "direct" cavity feeding is often used in the literature [104–107], where photons are directly generated in the cavity mode by an inverse cavity loss term. Such a feeding mechanism, acting together with the cavity loss, gives rise to a thermal photonic state with a temperature defined by the cavity-pump-to-loss ratio. This overlooks the fact that the background photons are generated through exciting an active medium, and hence are expected to have a coherent component [88]. On the other hand, detuned emitters can be explicitly included in the calculation, and their coupling to a detuned cavity mode via phonon or Auger coupling is facilitated by an effective system-bath coupling (Lindblad) term.This approach has the advantage that properties of the gain medium are preserved. The resulting cavity feeding is strongly non-linear with pump rate and exhibits saturation if the number of detuned emitters is limited. Furthermore, the overall emission can become coherent if the background contributions drive the laser above the threshold [88].

As an example, the left part of Figure 48.21 [108] shows the spectrum of a few-QD photonic-crystal nanocavity laser. Only few discrete QD lines are found in the vicinity of the mode (M1). The input–output characteristics is that of a nanolaser with a slight kink, hinting at a β-factor close to unity (middle panel), and coherent emission with $g^{(2)}(0) = 1$ being reached (right panel). Remarkably, the performance of the device is insensitive to tuning of the cavity-mode energy, which can be realized by gas deposition on the photonic crystal cavity. Evidence for this is found in the autocorrelation function in the right panel, which shows a clear transition to lasing with $g^{(2)}(0) = 1$ *independently* of the exact cavity position. In a system with few discrete emission channels this provides strong evidence for the importance of nonresonant coupling effects. Similar results have been reported in [109], to which the authors referred to as "self-tuning gain" effect. Moreover, in the spontaneous emission regime the coupling of various multiexcitonic emission channels from different emitters inside the cavity leads to super-thermal photon bunching with $g^{(2)}(0) > 2$. A density-matrix theory including quantum-mechanical correlations between these transitions, shown as green curve in the right panel, is in good agreement with the measured data. Neither rate equations, nor conventional laser models can unravel the intricate quantum-mechanical nature that governs the laser properties of few-emitter cavity-QED systems.

48.9 Outlook

With present-day nanolaser devices, we are closer than ever to reaching fundamental limits of light–matter interaction in semiconductor systems. Electronic excitations can be generated and used on the level of single excitons [110,111]. Brought into interaction with a single mode of microresonator, semiconductor nanolasers operate at the transition to the regime of quantum optics, where cavity-QED effects, such as photon blockade, photon-antibunching, and vacuum Rabi oscillations can coexist with lasing in different excitation regimes of the same device [105,112]. This offers fascinating prospects both from a fundamental and an applied point of view.

Acknowledgments

The authors would like to thank Joachim Piprek for the kind invitation to write this chapter. We also thank Andreas Beuthner for his help in creating the schematic figures. The Bremen group acknowledges financial support from the German Science Foundation (DFG).

Sandia National Laboratories is a multimission laboratory managed and operated by National Technology and Engineering Solutions of Sandia, LLC., a wholly owned subsidiary of Honeywell International, Inc., for the U.S. Department of Energy's National Nuclear Security Administration under contract DE-NA-0003525. WWC thanks the hospitality of the Technical University Berlin and travel support from the German Research Foundation via the collaborative research center 787.

References

1. Vahala, K. J. (2003). Optical microcavities. *Nature 424* (6950), 839–846.
2. Borri, P., W. Langbein, S. Schneider, U. Woggon, R. L. Sellin, D. Ouyang, and D. Bimberg (2002). Relaxation and dephasing of multiexcitons in semiconductor quantum dots. *Physical Review Letters 89* (18), 187401.
3. Borri, P., W. Langbein, U. Woggon, V. Stavarache, D. Reuter, and A. D. Wieck (2005). Exciton dephasing via phonon interactions in InAs quantum dots: Dependence on quantum confinement. *Physical Review B 71* (11), 115328.
4. Florian, M., A. Steinhoff, C. Gies, and F. Jahnke (2016). Scattering-induced dephasing of many-particle transitions in semiconductor quantum dots. *Applied Physics B 122* (1), 1–7.
5. Blood, P. (2013). The laser diode: 50 years on. *IEEE Journal of Selected Topics in Quantum Electronics 19* (4), 1503201–1503201.
6. Ning, C. (2013). What is laser threshold? *IEEE Journal of Selected Topics in Quantum Electronics 19* (4), 1503604–1503604.
7. Rice, P. R. and H. J. Carmichael (1994). Photon statistics of a cavity-QED laser: A comment on the laser–phase-transition analogy. *Physical Review A 50* (5), 4318–4329.
8. Chow, W. W., M. Lorke, and F. Jahnke (2011). Will quantum dots replace quantum wells as the active medium of choice in future semiconductor lasers? *IEEE Journal of Selected Topics in Quantum Electronics 17*, 1349–1355.
9. Yokoyama, H. and S. D. Brorson (1989). Rate equation analysis of microcavity lasers. *Journal of Applied Physical 66*, 4801.
10. Musiał, A., C. Hopfmann, T. Heindel, C. Gies, M. Florian, H. A. M. Leymann, A. Foerster, C. Schneider, F. Jahnke, S. Höfling, M. Kamp, and S. Reitzenstein (2015). Correlations between axial and lateral emission of coupled quantum dot micropillar cavities. *Physical Review B 91* (20), 205310.
11. Munsch, M., N. S. Malik, E. Dupuy, A. Delga, J. Bleuse, J.-M. Gérard, J. Claudon, N. Gregersen, and J. Mørk (2013). Dielectric GaAs antenna ensuring an efficient broadband coupling between an InAs quantum dot and a Gaussian optical beam. *Physical Review Letters 110* (17), 177402.
12. Leymann, H. A. M., C. Hopfmann, F. Albert, A. Foerster, M. Khanbekyan, C. Schneider, S. Höfling, A. Forchel, M. Kamp, J. Wiersig, and S. Reitzenstein (2013). Intensity fluctuations in bimodal micropillar lasers enhanced by quantum-dot gain competition. *Physical Review A 87* (5), 053819.
13. Agrawal, G. P. and N. K. Dutta (1993). *Semiconductor Laser*. Norwell, MA: Kluwer.
14. Chuang, S. L. (1995). *Physics of Optoelectronic Devices*. New York, NY: Wiley.
15. Lohmeyer, H., K. Sebald, C. Kruse, R. Kröger, J. Gutowski, D. Hommel, J. Wiersig, N. Baer, and F. Jahnke (2006). Confined optical modes in monolithic II-VI pillar microcavities. *Applied Physics Letters 88* (5), 051101.
16. McCall, S. L., A. F. J. Levi, R. E. Slusher, S. J. Pearton, and R. A. Logan (1992). Whispering gallery mode microdisk lasers. *Applied Physics Letters 60* (3), 289–291.
17. Joannopoulos, J. D., P. R. Villeneuve, and S. Fan (1997). Photonic crystals: Putting a new twist on light. *Nature 386* (6621), 143–149.
18. Purcell, E. M. (1946). Spontaneous emission probability at radio frequencies. *Physical Review 69*, 681.

19. Schwab, M., H. Kurtze, T. Auer, T. Berstermann, M. Bayer, J. Wiersig, N. Baer, C. Gies, F. Jahnke, J. P. Reithmaier, A. Forchel, M. Benyoucef, and P. Michler (2006). Radiative emission dynamics of quantum dots in a single cavity micropillar. *Physical Review B 74* (4), 045323.
20. Aßmann, M., F. Veit, M. Bayer, M. v. d. Poel, and J. M. Hvam (2009). Higher-order photon bunching in a semiconductor microcavity. *Science 325* (5938), 297–300. PMID: 19608912.
21. Loudon, R. (2000). *The Quantum Theory of Light*. Oxford, UK: Oxford University Press.
22. Hanbury Brown, R. and R. Q. Twiss (1956). Correlation between photons in two coherent beams of light. *Nature 177*, 27–29.
23. Ulrich, S. M., C. Gies, J. Wiersig, S. Reitzenstein, C. Hofmann, A. Löffer, A. Forchel, F. Jahnke, and P. Michler (2007). Photon statistics of semiconductor microcavity lasers. *Physical Review Letters 98*, 043906.
24. Gardiner, C. and P. Zoller (2004). *Quantum Noise A Handbook of Markovian and Non-Markovian Quantum Stochastic Methods with Applications to Quantum Optics*. Heidelberg, Berlin, New York: Springer Verlag.
25. Gies, C., M. Florian, P. Gartner, and F. Jahnke (2012). Modelling single quantum dots in microcavities. In F. Jahnke (Ed.), *Quantum Optics with Semiconductor Nanostructures*. Philadelphia, PA: Woodhead Publishing Limited.
26. Ates, S., C. Gies, S. M. Ulrich, J. Wiersig, S. Reitzenstein, A. Löffler, A. Forchel, F. Jahnke, and P. Michler (2008). Influence of the spontaneous optical emission factor β on the first-order coherence of a semiconductor microcavity laser. *Physical Review B 78* (15), 155319.
27. Chow, W. W., F. Jahnke, and C. Gies (2014). Emission properties of nanolasers during the transition to lasing. *Light: Science & Applications 3* (8), e201.
28. Ritter, S., P. Gartner, C. Gies, and F. Jahnke (2010). Emission properties and photon statistics of a single quantum dot laser. *Optics Express 18* (10), 9909–9921.
29. Reitzenstein, S., C. Böckler, A. Bazhenov, A. Gorbunov, A. Löffer, M. Kamp, V. D. Kulakovskii, and A. Forchel (2008). Single quantum dot controlled lasing effects in high-q micropillar cavities. *Optics Express 16* (7), 4848–4857.
30. Gies, C., J. Wiersig, and F. Jahnke (2008). Output characteristics of pulsed and continuous-wave-excited quantum-dot microcavity lasers. *Physical Review Letters 101* (6), 067401.
31. Chow, W. and S. Koch (2005). Theory of semiconductor quantum-dot laser dynamics. *IEEE Journal of Quantum Electronics 41* (4), 495–505.
32. Kolarczik, M., N. Owschimikow, J. Korn, B. Lingnau, Y. Kaptan, D. Bimberg, E. Schöll, K. Lüdge, and U. Woggon (2013). Quantum coherence induces pulse shape modification in a semiconductor optical amplifier at room temperature. *Nature Communications 4*, 2953.
33. Gies, C., J. Wiersig, M. Lorke, and F. Jahnke (2007). Semiconductor model for quantum-dot-based microcavity lasers. *Physical Review A 75* (1), 013803.
34. Wiersig, J., C. Gies, F. Jahnke, M. Aßmann, T. Bestermann, M. Bayer, C. Kistner, S. Reitzenstein, S. H. A. Forchel, C. Kruse, J. Kalden, and D. Hommel (2009). Direct observation of correlations between individual photon emission events of a microcavity laser. *Nature 460*, 245.
35. Baer, N., C. Gies, J. Wiersig, and F. Jahnke (2006). Luminescence of a semiconductor quantum dot system. *European Physical Journal B 50*, 411.
36. Gregersen, N., T. Suhr, M. Lorke, and J. Mørk (2012). Quantum-dot nano-cavity lasers with Purcell-enhanced stimulated emission. *Applied Physics Letters 100* (13), 131107.
37. Lermer, M., N. Gregersen, M. Lorke, E. Schild, P. Gold, J. Mørk, C. Schneider, A. Forchel, S. Reitzenstein, S. Hing, and M. Kamp (2013). High beta lasing in micropillar cavities with adiabatic layer design. *Applied Physics Letters 102* (5), 052114.
38. Lorke, M., T. Suhr, N. Gregersen, and J. Mørk (2013). Theory of nanolaser devices: Rate equation analysis versus microscopic theory. *Physical Review B 87*, 205310.

39. Suhr, T., N. Gregersen, M. Lorke, and J. Mørk (2011). Modulation response of quantum dot nanolightemitting-diodes exploiting Purcell-enhanced spontaneous emission. *Applied Physics Letters 98* (21), 211109.
40. Chow, W. and S. Koch (1999). *Semiconductor-Laser Fundamentals* (1st ed.). Berlin: Springer-Verlag.
41. Coldren, L. and S. Corzine (1995). *Diode Lasers and Photonic Integrated Circuits*. New York, NY: Wiley.
42. Binder, R., H. Köhler, M. Bonitz, and N. Kwong (1997). Green's function description of momentum orientation relaxation of photoexcited electron plasmas in semiconductors. *Physical Review B 55*, 5110.
43. Bonitz, M., D. Kremp, D. Scott, R. Binder, W. Kraeft, and H. Köhler (1996). Numerical analysis of nonmarkovian effects in charge-carrier scattering: One-time kinetic equations. *Journal of Physics: Condensed Mattter 8*, 6057.
44. ElSayed, K., S. Schuster, H. Haug, G. Herzel, and K. Henneberger (1994). Subpicosecond plasmon response: Buildup of screening. *Physical Review B 49*, 7337.
45. Henneberger, K. (1988). Resonant laser excitation and electron-hole kinetics of a semiconductor: I. nonequilibrium green's function treatment and fundamental equations. *Physica A 150*, 419.
46. Jahnke, F. and S. W. Koch (1995). Many-body theory for semiconductor microcavity lasers. *Physical Review A 52*, 1712.
47. Bányai, L., P. Gartner, and H. Haug (1998). Self-consistent RPA retarded polaron Green function for quantum kinetics. *European Physical Journal B 1*, 209.
48. Gartner, P., L. Bányai, and H. Haug (1999). Two-time electron-LO-phonon quantum kinetics and the generalized Kadanoff-Baym approximation. *Physical Review B 60*, 14234.
49. Gartner, P., L. Bányai, and H. Haug (2002). Self-consistent RPA for the intermediate-coupling polaron. *Physical Review B 66*, 75205.
50. Hartmann, M. and W. Schäfer (1992). Real time approach to relaxation and dephasing processes in semiconductors. *Physical Status Solidi (B) 173*, 165.
51. Haug, H. (1992). Interband quantum kinetics with LO-phonon scattering in a laser-pulse-excited semiconductor I. Theory. *Physical Status Solidi (B) 173*, 139.
52. Jahnke, F. and S. W. Koch (1993). Theory of carrier heating through injection pumping and lasing in semiconductor microcavity lasers. *Optics Letters 18* (17), 1438–1440.
53. Lorke, M., T. R. Nielsen, and J. Mørk (2011). Switch-on dynamics of nanocavity laser devices. *Applied Physics Letters 99* (15), 151110.
54. Lingnau, B., K. Lüdge, E. Schöll, and W. W. Chow (2010). Many-body and nonequilibrium effects on relaxation oscillations in a quantum-dot microcavity laser. *Applied Physics Letters 97*, 111102.
55. Lorke, M., T. R. Nielsen, and J. Mørk (2010). Influence of carrier dynamics on the modulation bandwidth of quantum-dot based nanocavity devices. *Applied Physics Letters 97* (21), 211106.
56. Luedge, K., M. J. P. Bormann, E. Malic, P. Hoevel, M. Kuntz, D. Bimberg, A. Knorr, and E. Schoell (2008). Turn-on dynamics and modulation response in semiconductor quantum dot lasers. *Physical Review B 78*, 035316.
57. Luedge, K. and E. Scholl (2009). Quantum-dot lasers—Desynchronized nonlinear dynamics of electrons and holes. *IEEE Journal of Quantum Electronics 45* (11), 1396–1403.
58. Aßmann, M., F. Veit, M. Bayer, C. Gies, F. Jahnke, S. Reitzenstein, S. Höfling, L. Worschech, and A. Forchel (2010). Ultrafast tracking of second-order photon correlations in the emission of quantum-dot microresonator lasers. *Physical Review B 81* (16), 165314.
59. Lorke, M., W. Chow, T. R. Nielsen, J. Seebeck, P. Gartner, and F. Jahnke (2006). Anomaly in the excitation dependence of optical gain in semiconductor quantum dots. *Physical Review B 74*, 035334.
60. Lorke, M., T. Nielsen, J. Seebeck, P. Gartner, and F. Jahnke (2006). Influence of carrier-carrier and carrier-phonon correlations on optical absorption and gain in quantum-dot systems. *Physical Review B 73*, 85324.

61. Schäfer, W. and M. Wegener (2002). *Semiconductor Optics and Transport Phenomena* (1st ed.). Berlin: Springer-Verlag.
62. Mahan, G. (1990). *Many-Particle Physics*. New York, NY: Plenum Press.
63. Seebeck, J., T. Nielsen, P. Gartner, and F. Jahnke (2005). Polarons in semiconductor quantum dots and their role in the quantum kinetics of carrier relaxation. *Physical Review B 71*, 125327.
64. Nielsen, T. R., P. Gartner, and F. Jahnke (2004). Many-body theory of carrier capture and relaxation in semiconductor quantum-dot lasers. *Physical Review B 69* (23), 235314.
65. Benisty, H. (1995). Reduced electron-phonon relaxation rates in quantum-box systems: Theoretical analysis. *Physical Review B 51*, 13281.
66. Inoshita, T. and H. Sakaki (1996). Electron-phonon interaction and the so-called phonon bottleneck effect in semiconductor quantum dots. *Physica B 227*, 373.
67. Kurtze, H., J. Seebeck, P. Gartner, D. R. Yakovlev, D. Reuter, A. D. Wieck, M. Bayer, and F. Jahnke (2009). Carrier relaxation dynamics in self-assembled semiconductor quantum dots. *Physical Review B 80*, 235319.
68. Schuh, K., F. Jahnke, and M. Lorke (2011). Rapid adiabatic passage in quantum dots: Influence of scattering and dephasing. *Applied Physics Letters 99* (1), 011105.
69. Seebeck, J., T. Nielsen, P. Gartner, and F. Jahnke (2006). Quantum kinetic theory of phonon-assisted carrier transitions in nitride-based quantum-dot systems. *European Physical Journal B 49*, 167.
70. Seebeck, J., M. Lorke, P. Gartner, and F. Jahnke (2009). Carrier-carrier and carrier-phonon scattering in the low-density and low-temperature regime for resonantly pumped semiconductor quantum dots. *Physica Status Solidi (C) 6*, 488.
71. Uskov, A. V., C. Meuer, H. Schmeckebier, and D. Bimberg (2011). Auger capture induced carrier heating in quantum dot lasers and amplifiers. *Applied Physics Express 4* (2), 022202.
72. Goldmann, E., M. Lorke, T. Frauenheim, and F. Jahnke (2014). Negative differential gain in quantum dot systems: Interplay of structural properties and many-body effects. *Applied Physics Letters 104* (24), 242108.
73. Lorke, M., W. Chow, and F. Jahnke (2007). Reduction of optical gain in semiconductor quantum dots. *Proceedings of SPIE 6468*, 646818.
74. Lorke, M., F. Jahnke, and W. Chow (2007). Excitation dependence of gain and carrier induced refractive index changes in quantum dots. *Applied Physical Letters 90*, 51112.
75. Lorke, M., J. Seebeck, T. Nielsen, P. Gartner, and F. Jahnke (2006). Excitation dependence of the homogeneous linewidths in quantum dots. *Physical Status Solidi (C) 3*, 2393–2396.
76. Dicke, R. H. (1954). Coherence in spontaneous radiation processes. *Physical Review 93*, 99–110.
77. Mandel, L. and E. Wolf (1995). *Optical Coherence and Quantum Optics*. New York, NY: Cambridge University Press.
78. Bohnet, J. G., Z. Chen, J. M. Weiner, D. Meiser, M. J. Holland, and J. K. Thompson (2012). A steady-state superradiant laser with less than one intracavity photon. *Nature 484* (7392), 78–81.
79. Timothy Noe Ii, G., J.-H. Kim, J. Lee, Y. Wang, A. K. Wójcik, S. A. McGill, D. H. Reitze, A. A. Belyanin, and J. Kono (2012). Giant superfluorescent bursts from a semiconductor magneto-plasma. *Nature Physics 8* (3), 219–224.
80. Leymann, H. A. M., A. Foerster, F. Jahnke, J. Wiersig, and C. Gies (2015). Sub—And superradiance in nanolasers. *Physical Review Applied 4* (4), 044018.
81. Auffèves, A., D. Gerace, S. Portolan, A. Drezet, and M. F. Santos (2011). Few emitters in a cavity: From cooperative emission to individualization. *New Journal of Physics 13* (9), 093020.
82. Jahnke, F., C. Gies, M. Aßmann, M. Bayer, H.A.M. Leymann, A. Foerster, J. Wiersig, C. Schneider, M. Kamp, and S. Höfling (2016). Giant photon bunching, superradiant pulse emission and excitation trapping in quantum-dot nanolasers. *Nature Communications 7*, 11540.
83. Bimberg, D., M. Grundmann, and N. N. Ledentsov (1998). *Quantum Dot Heterostructures*. Hoboken, NJ: John Wiley & Sons.

84. Bayer, M. and A. Forchel (2002). Temperature dependence of the exciton homogeneous linewidth in In0.60Ga0.40As/GaAs self-assembled quantum dots. *Physical Review B 65* (4), 041308.
85. Moody, G., R. Singh, H. Li, I. A. Akimov, M. Bayer, D. Reuter, A. D. Wieck, and S. T. Cundiff (2013). Fifth-order nonlinear optical response of excitonic states in an InAs quantum dot ensemble measured with two-dimensional spectroscopy. *Physical Review B 87* (4), 045313.
86. Scheibner, M., T. Schmidt, L. Worschech, A. Forchel, G. Bacher, T. Passow, and D. Hommel (2007). Superradiance of quantum dots. *Nature Physics 3* (2), 106–110.
87. Ates, S., S. M. Ulrich, A. Ulhaq, S. Reitzenstein, A. Löffler, S. Höfling, A. Forchel, and P. Michler (2009). Non-resonant dot—Cavity coupling and its potential for resonant single-quantum-dot spectroscopy. *Nature Photonics 3* (12), 724–728.
88. Florian, M., P. Gartner, C. Gies, and F. Jahnke (2013). Phonon-mediated off-resonant coupling effects in semiconductor quantum-dot lasers. *New Journal of Physics 15* (3), 035019.
89. Hohenester, U., A. Laucht, M. Kaniber, N. Hauke, A. Neumann, A. Mohtashami, M. Seliger, M. Bichler, and J. J. Finley (2009). Phonon-assisted transitions from quantum dot excitons to cavity photons. *Physical Review B 80* (20), 201311.
90. Majumdar, A., E. D. Kim, Y. Gong, M. Bajcsy, and J. Vučković (2011). Phonon mediated off-resonant quantum dot–cavity coupling under resonant excitation of the quantum dot. *Physical Review B 84* (8), 085309.
91. Press, D., S. Götzinger, S. Reitzenstein, C. Hofmann, A. Löffler, M. Kamp, A. Forchel, and Y. Yamamoto (2007). Photon antibunching from a single quantum-dot-microcavity system in the strong coupling regime. *Physical Review Letters 98* (11), 117402.
92. Tarel, G. and V. Savona (2009). Emission spectrum of a quantum dot embedded in a nanocavity. *Physica Status Solidi (C) 6* (4), 902–905.
93. Roy, C. and S. Hughes (2011). Influence of electron–acoustic-phonon scattering on intensity power broadening in a coherently driven quantum-dot–cavity system. *Physical Review X 1* (2), 021009.
94. Chauvin, N., C. Zinoni, M. Francardi, A. Gerardino, L. Balet, B. Alloing, L. H. Li, and A. Fiore (2009). Controlling the charge environment of single quantum dots in a photonic-crystal cavity. *Physical Review B 80* (24), 241306.
95. Florian, M., P. Gartner, A. Steinhoff, C. Gies, and F. Jahnke (2014). Coulomb-assisted cavity feeding in nonresonant optical emission from a quantum dot. *Physical Review B 89* (16), 161302(R).
96. Karrai, K., R. J. Warburton, C. Schulhauser, A. Högele, B. Urbaszek, E. J. McGhee, A. O. Govorov, J. M. Garcia, B. D. Gerardot, and P. M. Petroff (2004). Hybridization of electronic states in quantum dots through photon emission. *Nature 427* (6970), 135–138.
97. Settnes, M., P. Kaer, A. Moelbjerg, and J. Mork (2013). Auger processes mediating the nonresonant optical emission from a semiconductor quantum dot embedded inside an optical cavity. *Physical Review Letters 111* (6), 067403.
98. Winger, M., T. Volz, G. Tarel, S. Portolan, A. Badolato, K. J. Hennessy, E. L. Hu, A. Beveratos, J. Finley, V. Savona, and A. Imamoğlu (2009). Explanation of photon correlations in the far-off-resonance optical emission from a quantum-dot–cavity system. *Physical Review Letters 103* (20), 207403.
99. Bockelmann, U. and T. Egeler (1992). Electron relaxation in quantum dots by means of auger processes. *Physical Review B 46*, 15574.
100. Efros, A. L., V. A. Kharchenko, and M. Rosen (1995). Breaking of the phonon bottleneck in nanometer quantum dots role of auger-like processes. *Solid State Communications 93*, 281.
101. Uskov, A. V., F. Adler, H. Schweizer, and M. H. Pilkuhn (1997). Auger carrier relaxation in self-assembled quantum dots by collisions with two-dimensional carriers. *Journal of Applied Physics 81*, 7895.
102. Dekel, E., D. Gershoni, E. Ehrenfreund, D. Spektor, J. M. Garcia, and P. M. Petroff (1998). Multiexciton spectroscopy of a single self-assembled quantum dot. *Physical Review Letters 80* (22), 4991–4994.

103. Laucht, A., M. Kaniber, A. Mohtashami, N. Hauke, M. Bichler, and J. J. Finley (2010). Temporal monitoring of nonresonant feeding of semiconductor nanocavity modes by quantum dot multiexciton transitions. *Physical Review B 81*, 241302.
104. del Valle, E., F. P. Laussy, and C. Tejedor (2009). Luminescence spectra of quantum dots in microcavities. II. Fermions. *Physical Review B 79*, 235326.
105. Nomura, M., N. Kumagai, S. Iwamoto, Y. Ota, and Y. Arakawa (2010). Laser oscillation in a strongly coupled single-quantum-dot–nanocavity system. *Nature Physics 6*, 279–283.
106. Valle, E. d. and F. P. Laussy (2011). Effective cavity pumping from weakly coupled quantum dots. *Superlattices and Microstructures 49* (3), 241–245.
107. Yao, P., P. K. Pathak, E. Illes, S. Hughes, S. Münch, S. Reitzenstein, P. Franeck, A. Löffer, T. Heindel, S. Höfling, L. Worschech, and A. Forchel (2010). Nonlinear photoluminescence spectra from a quantum-dot cavity system: Interplay of pump-induced stimulated emission and anharmonic cavity QED. *Physical Review B 81* (3), 033309.
108. Lichtmannecker, S., M. Florian, T. Reichert, M. Blauth, M. Bichler, F. Jahnke, J. J. Finley, C. Gies, and M. Kaniber (2016). A few-emitter solid-state multi-exciton laser. *ArXiv:1602.03998 [condmat]*.
109. Strauf, S., K. Hennessy, M. T. Rakher, Y.-S. Choi, A. Badolato, L. C. Andreani, E. L. Hu, P. M. Petroff, and D. Bouwmeester (2006). Self-tuned quantum dot gain in photonic crystal lasers. *Physical Review Letters 96*, 127404.
110. Mlynek, J. A., A. A. Abdumalikov, C. Eichler, and A. Wallraff (2014). Observation of Dicke superradiance for two artificial atoms in a cavity with high decay rate. *Nature Communications 5*, 5186.
111. Müller, M., S. Bounouar, K. D. Jöns, M. Glässl, and P. Michler (2014). On-demand generation of indistinguishable polarization-entangled photon pairs. *Nature Photonics 8* (3), 224–228.
112. Muñoz, C. S., E. del Valle, A. G. Tudela, K. Müller, S. Lichtmannecker, M. Kaniber, C. Tejedor, J. J. Finley, and F. P. Laussy (2014). Emitters of n-photon bundles. *Nature Photonics 8* (7), 550–555.